Chapter 1: Introduction to electron paramagnetic resonance

1.1 Summary

This chapter contains a brief overview of electron paramagnetic resonance (EPR) theory. The contents are limited to the principles underlying EPR of nitroxides that have been attached to proteins *via* site-directed spin labeling (SDSL). For a more complete treatment of magnetic resonance theory, the reader is referred elsewhere (1-4). The present discussion begins with a description of the SDSL technique and the nitroxide-containing label R1 used in this dissertation, followed by examples from the literature that illustrate the ability of SDSL EPR to report local protein dynamics. Next, a description of the basic resonance condition and relaxation theory general to EPR spectroscopy is presented. The focus is then narrowed to nitroxides, in particular the structural aspects of nitroxides that influence the spectral lineshape. Then, a spectral simulation method for analyzing the motional dependence of the lineshape of nitroxide-labeled proteins in solution is described. Finally, the double electron-electron resonance (DEER) technique for determining inter-spin distances in doubly-labeled proteins is introduced.

1.2 Site-directed spin labeling

The concept of an environmentally sensitive "reporter" group targeted and covalently attached to a specific protein residue *via* a "positioning" group was introduced by Koshland for the purpose of monitoring functionally relevant changes in protein structure (5). This concept was extended to electron paramagnetic resonance (EPR) a year later by McConnell (6), where the idea of incorporating stable free radicals into proteins to serve as reporter groups for EPR was introduced in a method termed "spin labeling." Nitroxide derivatives were the first spin labels used in EPR spectroscopy, and are still by far the most common, although other stable radicals have been used (7-10). Nitroxides are stable over a pH range of 3-10 and temperatures

up to 80^{o}C (11). Quaternary carbons at the neighboring bonds protect the radical from disproportionation reactions (12), and incorporation of the nitroxide group into a ring structure (six-membered piperidine or five-membered pyrrole) limits the flexibility of the nitroxide. One potential limitation is that nitroxide-containing spin labels are susceptible to reduction to the diamagnetic (EPR silent) form by mild reducing agents (13).

One option for spin-labeling the protein of interest is to label native residues. Functional groups with specific reactivity for a particular amino acid side chain allow covalent attachment of spin labels. Maleimide and methanethiosulfonate groups react with cysteine residues, while hydroxylsuccinimide reacts with lysines. Lysine residues are typically more abundant than cysteines, therefore cysteines are usually preferred in order to provide more specific, localized information in the EPR spectrum. Even though different positioning groups allow some versatility with respect to the incorporation of spin labels into proteins, the limitation to naturally occurring residues and the inability to select one site from among all cysteine or lysine locations was a significant limitation to early applications of EPR in proteins.

Development of site-directed mutagenesis and recombinant protein expression and purification techniques in the late 1980s provided the groundwork for a major advancement in biophysical EPR, wherein spin labels could be introduced site-specifically into any recombinant protein in a technique pioneered by Hubbell (14) known as site-directed spin labeling (SDSL). This is shown schematically in Figure 1.1A, where a native residue is mutated to a cysteine, which is then reacted with a nitroxide derivative to generate a nitroxide side chain.

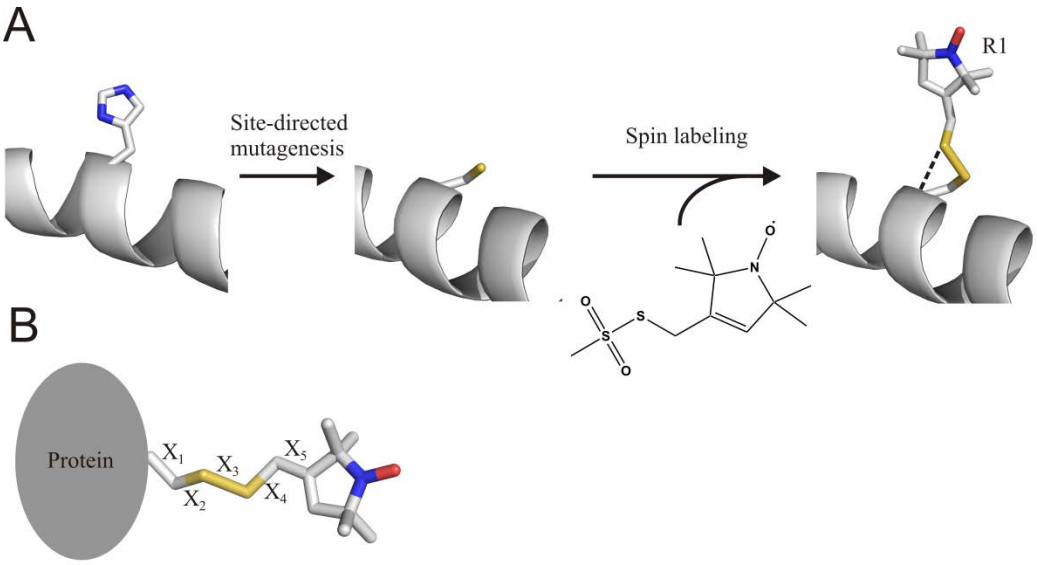

Figure 1.1 Site-directed spin labeling. (A) A native residue (left panel) is mutated to cysteine (center panel). The mutant is expressed and purified, and then a sulfhydryl-specific nitroxide-containing reagent is reacted with the protein to generate a spin label side chain (right panel). In the example shown here, a native histidine is mutated to a cysteine, and a methanethiosulfonate spin label reagent reacts with the cysteine to generate an R1 side chain linked to the protein through a disulfide bond. The dashed line indicates the intraresidue S_δ-HC_α bond that restricts rotation about the first two side chain bonds. (B) Designations of the five dihedral angles of R1 discussed in the text.

The nitroxide side chain used almost exclusively in the work presented in this dissertation is that designated R1 (Figure 1.1), utilized by reaction of 2,2,5,5-tetramethyl-pyrroline-1-oxyl methanethiosulfonate with the thiol of a cysteine to generate a nitroxide side chain covalently attached to the protein *via* a disulfide linkage. This commonly used spin label is well-characterized (15, 16) and advantages of the R1 label as a probe of protein dynamics include its relatively small size, with a molecular volume comparable to tryptophan, and its relatively flexible linker, which helps minimize perturbations to the protein structure and stability. The effect of R1 on protein structure and stability has been extensively studied and found to be minimal, particularly for solvent-exposed surface sites (7, 15) like those used in this dissertation. A potential disadvantage to thiol-reactive labels is the necessity for eliminating native cysteines by replacement with alanine or serine. This is not an issue for the two proteins studied in this

dissertation, but alternative strategies based on the incorporation of unnatural amino acids with bio-orthogonal groups for site-specific labeling are available (17, 18).

As discussed in the following sections of this chapter, the EPR spectrum is highly sensitive to motion of the nitroxide on the ns time scale, which contains contributions from protein rotary diffusion, local backbone fluctuations, and internal motion of the nitroxide side chain. In this dissertation, molecular motions are quantified in terms of a rotational correlation time τ unless specified otherwise. τ is related to the diffusion coefficient for molecular motion and indicates the characteristic time scale for fluctuations. Generally, a correlation time is the characteristic time for decay of an autocorrelation function. For isotropic rotational Brownian motion, τ is defined as $1/6D$, where D is the spherical diffusion coefficient (4). The rotary diffusion of the protein makes a negligible contribution for membrane-bound proteins and soluble proteins with MW $\gtrsim$ 50 kDa, and may be minimized for smaller soluble proteins by increasing the effective viscosity of the solution or site-specific attachment to a solid support (19, 20).

The two remaining contributions to the motion of the nitroxide group are local backbone fluctuations and internal side chain motion. Ultimately the primary interest lies in local protein structure and dynamics, and interpretation of EPR spectra in terms of protein motion generally requires knowledge of the internal dynamics of the spin label side chain. In principle, internal motion of the spin label side chain may be reduced by developing more rigid and/or bulkier spin labels, but in practice a certain degree of flexibility in the spin label helps avoid distorting the native protein structure as mentioned above. The structural basis for spin label motion is best understood for R1 at solvent-exposed surface sites on helices and loops, wherein density functional calculations (16) and high-resolution crystal structures of spin-labeled T4 lysozyme

(15), Spa15 (21), CylR2 (22), KcsA (23), and LeuT (24) have demonstrated a ubiquitous intra-residue hydrogen bond (S_δ-HC_α) in R1 that restricts rotational motion about the first two bonds ($\mathbf{X}_1$ and $\mathbf{X}_2$, Figure 1.1). This, in combination with the restriction in $\mathbf{X}_3$ due to the rotational barrier common to disulfide bonds (25), results in anisotropic motion of the nitroxide due to rotation about $\mathbf{X}_4$ and $\mathbf{X}_5$. This "$\mathbf{X}_4/\mathbf{X}_5$ model" was originally proposed based on analysis of solution-based EPR measurements of T4 lysozyme using spin labels with various side chain structures (9), and is supported by earlier mutational analysis and side chain structure variation experiments (7, 8). Spin label dynamics in β structures are complicated by the increased propensity for interactions with neighboring residues, but progress has been made in the recent reporting of crystal structures of spin-labeled soluble (26) and membrane-bound (27) β proteins.

Non-interacting surface sites on helices/loops exhibit site-independent internal motion, therefore site-to-site variation in motion is due to contributions from local backbone motion. This is strongly supported by comparison of SDSL EPR data with results from previous studies employing other techniques. A detailed discussion of the motional dependence of the EPR spectral lineshape is presented later in the chapter. Next, illustrative examples of the sensitivity of EPR to local protein dynamics are briefly reviewed, wherein variation in ns timescale motion reported by lineshape analysis matched expectations for local motion based on published results.

In the case of the basic leucine zipper of yeast transcription factor GCN4 (GCN4-58 bZip), ^{15}N relaxation NMR experiments identified a gradient of motion along the DNA-binding region corresponding to relatively large backbone motions involving fluctuations between helical and non-helical conformations (28). A series of 27 singly spin-labeled mutants of this protein yielded spectra with sharp resonance lines in the DNA-binding region, consistent with the local disorder identified in this sequence by NMR. Spectral simulations (29) and a semi-quantitative

measure of motion based on the central linewidth, referred to as the scaled mobility parameter, revealed that the site-specific variation in EPR spectral lineshape captured the same motional gradient first identified by NMR (30). This was a landmark demonstration of the contribution of backbone motion to the spectral lineshape. However, the backbone motion was relatively high amplitude in the DNA-binding region in which the motional gradient was observed and measured. This leaves an open question as to the contribution of smaller amplitude backbone fluctuations, e.g. helical rocking motions.

Although contribution of local backbone fluctuations to the EPR lineshape was reported previously (7, 9, 30, 31), the study of myoglobin by López et al. (32) provided an extensive and thorough demonstration that even subtle variations in backbone fluctuations are reflected in the spectral lineshape. In this study, 29 non-interacting surface sites on holomyoglobin were labeled with R1, one at a time. As with the GCN4-58 bZip study, the EPR spectra were analyzed using the scaled mobility parameter and spectral simulations. Site-specific variation in these EPR-based measures of motion was compared to the local fractional buried surface area to determine whether local backbone fluctuations contributed significantly to the EPR lineshape. This comparison operates under the assumption that as the buried surface area increases, the greater number of atomic contacts made by the helix will decrease its mobility. Remarkably, the EPR-based measures of motion were found to correlate well with local packing.

Interestingly, the H-helix in holomyoglobin exhibits a gradient of motion, with motion increasing from the N- to C-terminal end of the helix, based on crystallographic B-factors. In analogy with the GCN4-58 bZip study, the EPR spectra of sites in the H-helix of myoglobin reflected a gradient of motion consistent with expectations, although in the case of

holomyoglobin the motions consisted of small-amplitude backbone fluctuations within an intact helix.

The model for R1 motion and experimental results discussed above pertain to non-interacting surface sites. Contact and buried sites exhibit spectra reflective of highly restrictive motion due to interaction of the nitroxide with the local protein environment, and therefore the motion no longer follows the model for non-interacting sites. However, the dramatically different spectral lineshape due to interaction with the local environment makes the EPR spectrum an exquisitely sensitive probe of protein conformational exchange for properly placed residues (30, 32, 33), as discussed in detail in chapter 2.

The information presented in this section served to introduce the technique of SDSL EPR and the specific nitroxide spin label used in the work presented in this dissertation. In the following sections, the basic resonance condition and relaxation processes common to all EPR experiments will be covered. Then, the focus will narrow to theoretical and experimental aspects of EPR of spin-labeled proteins.

1.3 The resonance condition

The electron is a fermion (spin quantum number s = ½) with an intrinsic angular momentum, or spin angular momentum, denoted by S with a value of

$$S = \hbar\sqrt{s(s+1)} = \frac{\sqrt{3}}{2}\hbar \qquad [1.1]$$

where $\hbar$ is the reduced Planck constant and is equal to the Planck constant h divided by 2π. Electrons are charged particles, therefore the angular momentum gives rise to an electronic magnetic moment given by

$$\boldsymbol{\mu_e} = -g\beta_e\mathbf{S} \qquad [1.2]$$

where the vectors **S** (in units of $\hbar$) and $\boldsymbol{\mu_e}$ represent the electron angular momentum and magnetic moment, respectively. In [1.2], g is the electronic g-factor (g ≈ 2.002319 for a free electron), and β_e is the Bohr magneton

$$\beta_e = \frac{e\hbar}{2m} \qquad [1.3]$$

The collection of constants that comprise β_e are the rest mass of an electron m, the elementary charge e, and $\hbar$, defined above. β_e is positive using this definition, but the electron is negatively charged, therefore expression [1.2] includes a negative sign to indicate that the vector $\boldsymbol{\mu_e}$ is anti-parallel to the vector **S** (Figure 1.2). The total magnetic moment of an electron bound to a nucleus contains contributions from the spin term defined in [1.2] and an analogous orbital angular momentum term, but for organic radicals such as nitroxides the orbital angular momentum is largely quenched (34). In such cases, $\boldsymbol{\mu_e}$ and **S** are anti-parallel as specified by [1.2] and deviations in the value of g from that of a free electron account for the contribution of the orbital angular momentum from spin-orbit coupling. An orbital magnetic moment that is not aligned perfectly with the spin magnetic moment generates g-anisotropy that is accounted for by employing a tensor representation for g, as described in section **1.5**.

The interaction energy E of a magnetic dipole moment $\boldsymbol{\mu}$ in a magnetic field $\mathbf{H_0}$ is given by the dot product of the two vectors

$$E = -\boldsymbol{\mu} \cdot \mathbf{H_0} \qquad [1.4]$$

Combining [1.2] and [1.3] yields the energy of the interaction between electron spin angular momentum and an external field, termed the Zeeman interaction.

$$E = g\beta_e \mathbf{S} \cdot \mathbf{H_0} \qquad [1.5]$$

If the applied field $\mathbf{H_0}$ is uniform and along a single axis defined as z, the interaction energy is then proportional to S_z, the projection of **S** along the z-axis and [1.5] becomes

$$E = \frac{g\beta_e}{\hbar} S_z H_z \quad [1.6]$$

where

$$S_z = m_s \hbar \quad [1.7]$$

The secondary spin quantum number m_s can take one of $2s + 1$ values ranging from $+s$ to $-s$ in increments of one. For an electron $s = ½$ and therefore m_s can take two values, +½ and –½, generating two possible energies in [1.6]. It should be noted that the magnitude of **S** is fixed, and is defined by the value of the spin angular momentum given by [1.1]. The vector **S** (and thus $\boldsymbol{\mu_e}$) is not directly aligned with the z-axis defined by $\mathbf{H_0}$. The two possible spin states restrict **S** to two possible angles with respect to the z-axis, and therefore the projection of **S** along the z-axis can take one of two values. In the $m_s = +½$ state, the projection of **S** along the z-axis runs in the +z direction; this is referred to as the spin +½ state or the spin-up state. In the $m_s = –½$ state, S_z is along the –z direction; this is the spin –½ state or the spin-down state.

According to [1.6], the energy of the spin +½ state will be positive and the energy of the spin –½ state will be negative, relative to zero field where the energy associated with both orientations is zero (Figure 1.2). The energies of spin states defined in [1.6] assume all orientations of **S** are iso-energetic (degenerate) in the absence of an external field. This is not strictly true for systems with total spin quantum number >½, including the nitroxides considered here wherein the unpaired electron is bound to a nucleus with spin = 1, and there is a splitting of energy levels even at zero field (i.e., zero field splitting). Additional contributions to spin state energies in the high-field limit will be considered in section **1.5**, but this section is limited to the interaction of an electron spin with an applied magnetic field.

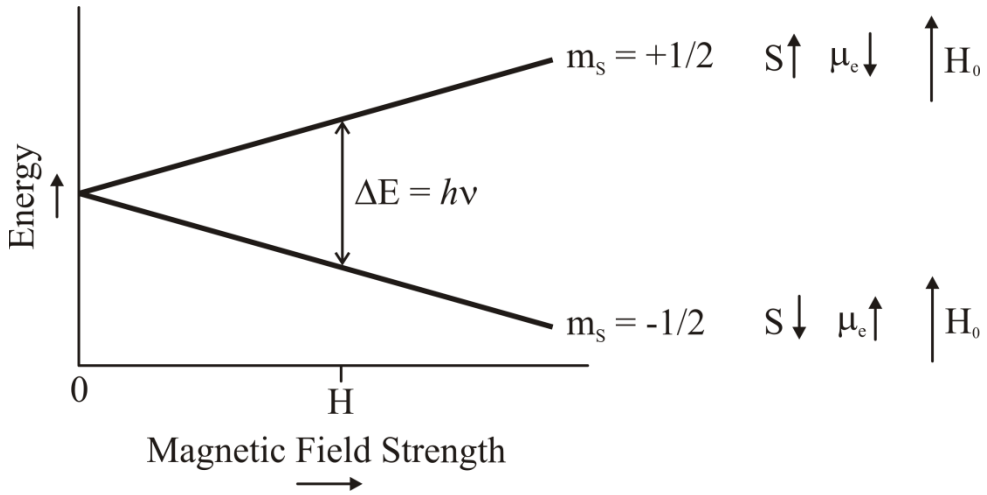

Figure 1.2 The basic resonance condition for an isolated electron spin. The energy separation between the two spin states increases linearly with magnetic field strength, and a transition between states may be stimulated if the indicated condition for radiation frequency and magnetic field is met (see [1.10]). On the right, arrows indicate the alignment of the projection of **S** and $\boldsymbol{\mu_e}$ on the axis of the external field $\mathbf{H_0}$ for each spin state.

Transitions between the spin +½ and spin –½ states can be induced by radiation of the proper frequency and polarization. The energy difference between the spin +½ and spin –½ states is

$$\Delta E = E\left(S_z = +\frac{1}{2}\hbar\right) - E\left(S_z = -\frac{1}{2}\hbar\right) = g\beta_e H_z \qquad [1.8]$$

The energy of radiation is proportional to its frequency according to the Planck relation

$$E = h\nu \qquad [1.9]$$

Therefore, the frequency of radiation required to excite a spin-state transition is given by

$$h\nu = g\beta_e H_z \qquad [1.10]$$

As indicated in [1.10], the frequency of radiation required to excite a transition is directly proportional to the magnitude of the applied field, illustrated graphically in Figure 1.2. The proportionality constants between field and frequency include h and β_e, which are invariant, and the g-factor, which depends on the particular system (see section **1.5**).

When the frequency and magnetic field are matched to induce a transition according to [1.10], time-dependent perturbation theory states that the radiation may be treated as a perturbation V(t) with the following probability of transition between states α and β:

$$P_{\alpha\beta} = \frac{2\pi}{\hbar}|\langle\beta|V|\alpha\rangle|^2\delta(\Delta E - h\nu) \qquad [1.11]$$

The Dirac delta $\delta(\Delta E - h\nu)$ serves to impose the requirement of [1.10] that the frequency of radiation match the energy difference between states, and $|\langle\beta|V|\alpha\rangle|^2$ represents the degree to which the states are mixed by the perturbation V(t) (4). The transition probability given by [1.11] is equivalent in either direction (i.e., $|\langle\beta|V|\alpha\rangle|^2 = |\langle\alpha|V|\beta\rangle|^2$), therefore for the two-state electron spin system under consideration here, the transition probability is equivalent for the transition from spin +½ to spin –½ and *vice versa*. A net absorption of radiation will therefore only occur if there is a difference in the population of spins in the two states.

A population difference is observed for an ensemble of spins in the presence of an applied field. The Boltzmann distribution law gives the relative population of spins in the +½ and –½ state at thermal equilibrium as a function of the energy separation between states,

$$\frac{N_+}{N_-} = e^{-\left(\Delta E/kT\right)} = e^{-\left(g\beta_e H_z/kT\right)} \qquad [1.12]$$

where N_+ is the number of spins in the +½ state, N_- is the number of spins in the –½ state, k is the Boltzmann constant, T is the temperature in Kelvin, and ΔE is the energy separation defined in [1.8]. As an example, consider the population difference anticipated at the commonly used X-band frequency, ≈ 9.5 GHz. This corresponds to a resonant field of ≈3400 Gauss, which yields a population ratio $\frac{N_+}{N_-}$ = 0.99847, or a difference of ≈0.08% in the equilibrium population of the two states at room temperature (298 K). As a side note, EPR uses radiation in the microwave frequency range and the different frequencies employed are often referred to using the frequency

band nomenclature originally developed during World War II. X-band is one commonly used frequency range; another is Q-band (≈35 GHz).

The transition between spin –½ and spin +½ states described above constitutes the fundamental spectroscopic transition measured in the EPR experiments reported in this dissertation. However, as implied by the introduction of [1.12], an ensemble of spins is monitored experimentally, and the description of this system developed by Bloch will be explored next.

1.4 The Bloch equations and magnetic relaxation

A phenomenological description of the behavior of an ensemble of spins in an applied field in terms of a single bulk magnetization vector **M** was developed by Felix Bloch in 1946 (1, 35). The time evolution of **M** is defined in the Bloch equations using the characteristic relaxation times T_1 and T_2. An abbreviated description of the Bloch equations is presented below, with the aim of illustrating two key results: the Lorentzian lineshape of the absorption spectrum, and the T_1 and T_2 dependence of the linewidth.

In classical electromagnetism, a magnetic dipole moment $\boldsymbol{\mu}$ in a magnetic field **H** experiences a torque given by $\boldsymbol{\mu} \times \mathbf{H}$, equal to the rate of change of its angular momentum $\frac{d\boldsymbol{\mu}}{dt}$. An electron possesses a magnetic moment proportional to its spin angular momentum as expressed in [1.2], and treating the electron magnetic moment classically yields

$$\frac{d\boldsymbol{\mu}_{\mathbf{e,i}}}{dt} = \gamma \boldsymbol{\mu}_{\mathbf{e,i}} \times \mathbf{H} \qquad [1.13]$$

where γ is the gyromagnetic ratio

$$\gamma = \frac{g\beta_e}{\hbar} \qquad [1.14]$$

The torque defined by [1.13] results in precession of $\boldsymbol{\mu}_{\mathbf{e,i}}$ about the axis of **H** with an angular frequency ω_0 known as the Larmor frequency, given by

$$\omega_0 = \gamma H \quad [1.15]$$

where H is the magnitude of the field. Expression [1.15] is equivalent to [1.10] with the ordinary frequency ν replaced by the angular frequency ω because the motion being described here is rotational. The two are related by

$$\omega = 2\pi\nu \quad [1.16]$$

where ν is in units of s^{-1} and ω is in units of rad* s^{-1}. Thus, the Larmor frequency is both the precession frequency of $\boldsymbol{\mu_{e,i}}$ and the angular frequency required to excite a transition for the energy level separation specified in [1.8]. The total electron magnetic moment, represented by the bulk magnetization vector **M**, is arrived at by a sum over all electrons in the ensemble.

$$\mathbf{M} = \sum \boldsymbol{\mu_{e,i}} \quad [1.17]$$

The motion of **M** in the presence of **H** is analogous to that of the individual $\boldsymbol{\mu_{e,i}}$.

$$\frac{d\mathbf{M}}{dt} = \gamma \mathbf{M} \times \mathbf{H} \quad [1.18]$$

H may be decomposed into two components,

$$\mathbf{H} = \mathbf{H_0} + \mathbf{H_1} \quad [1.19]$$

$\mathbf{H_0}$ is a large steady field applied along a single axis defined as z, and as discussed in section **1.2** it is responsible for splitting the energy levels of the spin states. $\mathbf{H_1}$ is an oscillatory field generated by microwave radiation with frequency defined in [1.8-10], and is usually weak for reasons presented below.

Expression [1.18] defines the rate of change of **M** due to the externally applied field **H**, but it doesn't account for relaxation processed due to internal fields within the sample. The contribution to the time evolution of **M** from relaxation may be defined with respect to the three principal axes x, y, and z using the following expressions:

$$\frac{dM_z}{dt} = -\frac{M_z - M_0}{T_1} \quad [1.20]$$

$$\frac{dM_y}{dt} = -\frac{M_y}{T_2} \quad [1.21]$$

$$\frac{dM_x}{dt} = -\frac{M_x}{T_2} \quad [1.22]$$

According to these expressions, magnetization along the z axis M_z will relax to its equilibrium value M_0 at a rate determined by the relaxation time constant T_1, and magnetization perpendicular to the large steady field $\mathbf{H_0}$ will relax to an equilibrium value of zero with the relaxation time constant T_2.

The time dependence of the bulk magnetization in the presence of the external fields $\mathbf{H_0}$ and $\mathbf{H_1}$ and relaxation mechanisms T_1 and T_2 is

$$\frac{d\mathbf{M}}{dt} = \gamma\mathbf{M} \times \mathbf{H_0} + \gamma\mathbf{M} \times \mathbf{H_1} - \frac{\mathbf{k}(M_z - M_0)}{T_1} - \frac{(\mathbf{i}M_x + \mathbf{j}M_y)}{T_2} \quad [1.23]$$

where **i**, **j**, and **k** are unit vectors in the x, y, and z direction. The torque imposed on **M** by the large uniform field $\mathbf{H_0}$ will result in clockwise precession about z when viewed along the positive z direction. In EPR experiments the $\mathbf{H_1}$ field oscillates with frequency ω_0 and is linearly polarized in a direction perpendicular to $\mathbf{H_0}$. $\mathbf{H_1}$ can be decomposed into two circularly polarized fields precessing in opposite directions, only one of which has a significant effect on the bulk electron magnetization because it precesses in the same direction and at the same frequency (i.e. is coherent). A solution to the Bloch equations is achieved using a transformation from a static frame of reference to a rotating frame defined by the circularly polarized component of $\mathbf{H_1}$ precessing in the clockwise direction, $\mathbf{H_1'}$. **M** is defined in the rotating coordinate system as

$$\mathbf{M} = \mathbf{i}'u + \mathbf{j}'v + \mathbf{k}'M_z \quad [1.24]$$

where $\mathbf{i}'$ is a unit vector in the same direction as $\mathbf{H_1'}$, $\mathbf{j}'$ is a unit vector in the xy-plane perpendicular to $\mathbf{i}'$, and $\mathbf{k}'$ is a unit vector pointing along the z-direction defined by $\mathbf{H_0}$ ($\mathbf{k}' = \mathbf{k}$) (Figure 1.3).

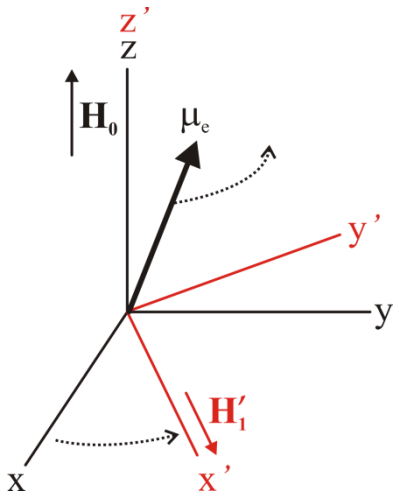

Figure 1.3 The static and rotating coordinate systems used in the Bloch relaxation equations. The static coordinate system is shown in black, with the z-axis defined by the direction of $\mathbf{H_0}$. The rotating coordinate system is shown in red, where the x' axis is defined by the direction of $\mathbf{H_1'}$ and the direction of precession is indicated by a dashed arrow. The magnitude of **M** projected along the x', y', and z' axes of the rotating system is u, v, and M_z, respectively. A magnetic moment vector $\boldsymbol{\mu_e}$ for a single electron spin is shown, and the dashed arrow indicates the precession direction. If the precession frequency of $\boldsymbol{\mu_e}$ matches that of $\mathbf{H_1'}$, a spin state transition may be induced.

The time evolution of u, v, and M_z is

$$\frac{du}{dt} = (\omega_0 - \omega)v - \frac{u}{T_2} \qquad [1.25]$$

$$\frac{dv}{dt} = -(\omega_0 - \omega)u + \gamma H_1 M_z - \frac{v}{T_2} \qquad [1.26]$$

$$\frac{dM_z}{dt} = -\gamma H_1 v - \frac{M_z - M_0}{T_1} \qquad [1.27]$$

The solution to these equations in the steady-state, where $\frac{du}{dt} = \frac{dv}{dt} = \frac{dM_z}{dt} = 0$, is

$$u = \frac{\gamma H_1 T_2^2 (\omega_0 - \omega) M_0}{1 + T_2^2(\omega_0 - \omega)^2 + \gamma^2 H_1^2 T_1 T_2} \qquad [1.28]$$

$$v = \frac{\gamma H_1 T_2 M_0}{1 + T_2^2(\omega_0 - \omega)^2 + \gamma^2 H_1^2 T_1 T_2} \qquad [1.29]$$

$$M_z = \frac{1 + T_2^2(\omega_0 - \omega)^2}{1 + T_2^2(\omega_0 - \omega)^2 + \gamma^2 H_1^2 T_1 T_2} \qquad [1.30]$$

The average power absorbed by the sample over one cycle of the $\mathbf{H_1'}$ field is

$$P(\omega) = \frac{\omega \gamma H_1^2 T_2 M_0}{1 + T_2^2(\omega_0 - \omega)^2 + \gamma^2 H_1^2 T_1 T_2} \qquad [1.31]$$

However, the recorded signal in most commercial EPR spectrometers is not the power absorbed by the sample, but rather the out-of-phase component of **M** in the rotating frame v. In the standard EPR experiment used to measure the resonance lineshape, $\mathbf{H_1'}$ is applied using

microwave radiation at a constant frequency and the large steady field $\mathbf{H_0}$ is slowly swept through the resonance line. This is referred to as a continuous-wave (CW) EPR spectrum, or simply an EPR spectrum. The signal v in terms of field-dependence is

$$v = \frac{\gamma H_1 \mathrm{T}_2 M_0}{1+\gamma^2 \mathrm{T}_2^2 (H_0 - H)^2 + \gamma^2 H_1^2 \mathrm{T}_1 \mathrm{T}_2} \quad [1.32]$$

where the signal maximum occurs when the applied field strength H matches the resonant field strength H_0. The absorption lineshape is Lorentzian (Figure 1.4A and B), and the full width at half-height $\Delta \mathrm{H}_{1/2}$ is

$$\Delta \mathrm{H}_{1/2} = \left[\frac{2}{\gamma \mathrm{T}_2}\right] \mathrm{s}^{-1/2} \quad [1.33]$$

where the saturation factor s is

$$\mathrm{s} = \frac{1}{1+\gamma^2 H_1^2 \mathrm{T}_1 \mathrm{T}_2} \quad [1.34]$$

Most EPR spectrometers employ field modulation (Figure 1.4A), therefore the signal recorded is the derivative $\frac{dv}{dH}$ where the peak-to-peak linewidth $\Delta \mathrm{H}_{\mathrm{pp}}$ is

$$\Delta \mathrm{H}_{\mathrm{pp}} = \left[\frac{2}{3^{1/2} \gamma \mathrm{T}_2}\right] \mathrm{s}^{-1/2} \quad [1.35]$$

The term $\gamma^2 H_1^2 \mathrm{T}_1 \mathrm{T}_2$ in [1.34] is small for weak H_1, and $\mathrm{s} \approx 1$ under these conditions. This is referred to as the non-saturating limit, and in this limit the linewidth given by [1.33] and [1.35] is dependent on T_2 but not T_1.

All CW EPR spectra reported in this dissertation were collected in the non-saturating limit. In this limit the signal is directly proportional to H_1 as indicated by [1.32]. Experimentally, it is the power of the microwave radiation used to generate H_1 that is controlled; the two are related by

$$H_1^2 = \mathrm{KP_w} \quad [1.36]$$

where K is a constant of order 1 and P_w is the microwave power (2). According to [1.36] and [1.32] the signal amplitude is directly proportional to $P_w^{1/2}$ in the non-saturating limit. At higher powers, the relaxation processes are not sufficiently fast to return the system to the equilibrium distribution of spins in the +½ and –½ state (as defined by the Boltzmann distribution [1.12]). When the power exceeds the non-saturating limit the saturation factor deviates from one, resulting in a non-linear dependence of the signal amplitude on $P_w^{1/2}$ and a dependence of the linewidth on T_1 and power instead of just T_2.

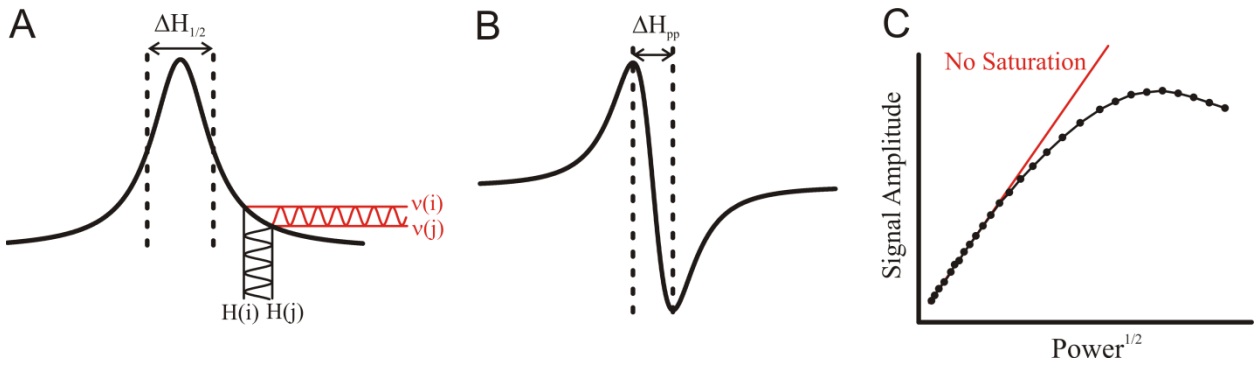

Figure 1.4 The Lorentzian lineshape, magnetic field modulation, and saturation effects. (A) The Lorentzian absorption lineshape is shown, with the full-width at half-height defined by [1.33] labeled. As the magnetic field strength is slowly swept through the resonance line, it is modulated at a fixed frequency with an amplitude given by H(j)-H(i). The amplitude of the signal v will oscillate between v(i) and v(j). (B) The detector monitors the signal at the frequency and phase set by the field modulation, resulting in the first-derivative lineshape shown. (C) Power saturation curve showing the behavior of the signal amplitude as power is increased, and the hypothetical signal amplitude in the absence of saturation (red).

A plot of signal amplitude vs. $P_w^{1/2}$ is called the power saturation curve (Figure 1.4C), and this illustrates the linear relationship at low powers and the reduction in signal amplitude at higher powers compared to the hypothetical non-saturated signal amplitude. A saturation curve may be used to determine the appropriate power range for measuring the CW EPR spectrum to avoid saturation. Alternatively, the saturation behavior may be utilized for determining T_1 and T_2 by measuring the signal amplitude and linewidth across a wide range of applied microwave

power, from the non-saturating to saturating regime (2). A direct measure of T_1 is possible using the saturation recovery method (36).

T_1 relaxation occurs through exchanges of energy between the spin and its surroundings that result in a transition from spin –½ to spin +½ or vice versa. As noted above, energy on the order of the separation between the two energy levels (i.e., radiation at the Larmor frequency) is required to induce such a transition. In early magnetic resonance experiments on crystalline solids, the degree to which the lattice thermal energy in the form of vibrations matched the energy of the spin transition was found to determine T_1 (1), thus this is often referred to as the spin-lattice relaxation time. Stronger coupling results in a more rapid return to equilibrium, therefore T_1 becomes shorter. In solution, mechanisms other than vibrational relaxation are known to be significant (37-41), but the relative contribution of the different mechanisms across different timescales of molecular motion, and a potential temperature-dependence separate from motional effects, is still unresolved.

In the non-saturating limit the Lorentzian linewidth is inversely proportional to T_2 according to [1.33] and [1.35], therefore identifying the factors contributing to T_2 relaxation is crucial for interpreting the spectral lineshape. Application of an oscillating field such as $\mathbf{H_1'}$ perpendicular to the z-axis can result in bulk magnetization vector components M_x and M_y having non-zero values, and the time constant for return of M_x and M_y to their equilibrium value of zero is T_2 as discussed above. Assume for the moment that a non-zero component of bulk magnetization is generated in the xy-plane, and then $\mathbf{H_1'}$ is no longer applied. If the only contribution to the magnetic field in the sample were the externally applied field $\mathbf{H_0}$ (and the field was perfectly homogeneous across the sample), all spins in the ensemble would then precess around the z-axis at exactly the same frequency, and the bulk magnetization component

in the xy-plane would precess about the z-axis indefinitely. However, variation in the local field at each spin causes the precession frequency to vary from spin-to-spin, and local field fluctuations will cause the precession frequency of each individual spin to vary as a function of time. Both effects will result in a loss of coherence (dephasing) of the precession about the z-axis and a return of M_x and M_y to their equilibrium values of zero. In addition to relaxation from local field fluctuations and/or variation, a T_2 relaxation can occur from direct spin-spin interactions *via* Heisenberg exchange, wherein two spins exchange magnetization during collision resulting in a loss of phase coherence (42).

Motional contributions dominate T_2 relaxation in solution, and originate from molecular tumbling that generates local field fluctuations. For example, in the spin-rotational mechanism molecular rotation results in a lag between the position of the electron and the nuclear framework to which it is attached, generating a magnetic moment that interacts with the electron spin through an intramolecular dipole-dipole interaction (43). The dipole-dipole (dipolar) interaction between the magnetic dipole moment of an electron and another dipole depends on the orientation of the vector joining the two with respect to the external field (44), therefore modulation of the dipolar interaction by molecular tumbling will generate local field fluctuations. Intermolecular dipolar interactions between electron spins and dipoles in surrounding solvent molecules may also contribute to T_2 relaxation. An additional mechanism related to orientation-dependence stems from anisotropy of the nitroxide g-factor and nitrogen hyperfine interaction (see section **1.5**). The orientation-dependence of these interactions means the electron spin will experience field fluctuations resulting from variation in these properties as the molecule tumbles in solution (4).

While T_1 and T_2 relaxation were introduced as distinct quantities representing separate processes, they are in fact related. Both T_1 and T_2 relaxation may be influenced by molecular motion, and Redfield theory provides a quantitative description of the dependence of T_1 and T_2 on the correlation time for isotropic rotational motion τ (3, 4, 45, 46). Redfield treated rotational tumbling using a random walk model, and derived the following expressions for T_1 and T_2 relaxation (3):

$$\frac{1}{T_1} = \gamma^2\left(\overline{H_x^2} + \overline{H_y^2}\right)\frac{\tau}{1+\omega_0^2\tau^2} \qquad [1.37]$$

$$\frac{1}{T_2} = \gamma^2\left[\overline{H_z^2}\tau + \frac{1}{2}\left(\overline{H_x^2} + \overline{H_y^2}\right)\frac{\tau}{1+\omega_0^2\tau^2}\right] \qquad [1.38]$$

According to these expressions, relaxation depends on γ, τ, the Larmor frequency ω_0, and the time-average squared fields $\overline{H_x^2}$, $\overline{H_y^2}$, and $\overline{H_z^2}$, which indicate the magnitude of the field fluctuations along the different axes of the static reference frame.

Field fluctuations along the x- and y-axis contribute to T_1 relaxation, and the magnitude of the contribution depends on the relative values of τ and ω_0 due to the $\omega_0^2\tau^2$ term in [1.37]. When rotational motion is much more rapid than Larmor precession (i.e. $\tau < \omega_0$) $1/T_1$ is proportional to τ, and when rotational motion is much slower than Larmor precession (i.e. $\tau > \omega_0$) $1/T_1$ is proportional to $1/\tau$. The right side of [1.37] is maximized when $\tau\omega_0 = 1$, meaning T_1 will reach a minimum when the inverse of the correlation time (i.e. rate of motion) is equivalent to the Larmor precession frequency. From a classical perspective, this result signifies that local field fluctuations which generate T_1 relaxation are those which induce a magnetic field in the xy-plane that precesses about the z-axis at the Larmor frequency. This is effectively a "static" field in the xy-plane from the perspective of a spin precessing about the z-axis at a matching frequency. As a result, precession is induced about the field in the xy-plane, changing

the net magnetization along z (T_1 relaxation); similar to $\mathbf{H_1'}$ defined above but highly localized (not uniform across the sample).

T_2 has a similar dependence to that of T_1 on fluctuating fields along the x- and y-axis, indicating that in addition to changing magnetization along the z-axis, these fluctuations cause dephasing of the precession about the z-axis (T_2 relaxation). In this respect, T_2 relaxation may be said to be influenced by T_1 relaxation. However, there is an additional term in expression [1.38] that indicates a dependence of T_2 on fluctuations along the z-axis. The z-axis contribution is influenced by τ but not ω_0, thus there is no minimum in T_2 predicted by Redfield theory. Instead, when $\tau > \omega_0$ the T_1-like term in [1.38] becomes negligible, T_2 relaxation is dominated by z-axis fluctuations, and $1/T_2$ is proportional to τ. Therefore, for rotational motion slower than the Larmor frequency, T_2 relaxation is not influenced by T_1 and the spectral linewidth defined by [1.33] and [1.35] is dependent on T_2 alone.

As mentioned above, Redfield theory uses a random-walk model for rotational motion, and field fluctuations due to the random walk cannot drive relaxation if relaxation occurs faster than a random-walk step. As τ increases, eventually it approaches equivalent values to T_2, and Redfield theory is no longer applicable. For nitroxide radicals in solution, Redfield theory is not applicable for τ longer than 1 ns, therefore it explains T_1 and T_2 relaxation for only a portion of the motional time window relevant to the EPR spectral lineshape as discussed in section **1.6**. At τ longer than the Redfield limit, other theoretical treatments and experimental observations have confirmed that T_1 remains much longer than T_2 (37, 38, 47-49). For nitroxide-labeled proteins in solution, T_1 ranges from ≈1-6 μs (36, 50) and T_2 ranges from ≈10-30 ns (2), such that T_1 makes only minimal contribution to the observed T_2.

1.5 The Spin Hamiltonian

In section **1.3**, the resonance condition for an isolated electron spin was discussed, and the resonant field position (i.e. magnetic field strength at which a spin transition will occur) was shown in [1.10] to be dependent on the frequency of radiation and the g-factor. The shape of the resonance line was described in section **1.4**, as well as the influence of relaxation on the linewidth. In both section **1.3** and **1.4**, the influence of attachment of the electron to a nucleus was not considered. For nitroxides the unpaired electron is bound to a nitrogen with spin quantum number $I = 1$ (^{14}N isotope, 99.6% natural abundance), the effects of which will be considered in this section.

As discussed in section **1.3**, the g-factor is a proportionality constant relating the frequency of radiation with the magnetic field of resonance for the Zeeman interaction between an electron spin and an applied magnetic field. For a free electron, the g-factor is ≈2.002319, but this value differs for electrons bound to a nucleus due to orbital angular momentum. The orbital angular momentum for nonlinear polyatomic free radicals like nitroxides is largely quenched (51), but spin-orbit coupling re-introduces a small orbital angular momentum (34), and the effect of the resulting magnetic moment is accounted for by variation in the g-factor. In this manner, the deviation of the g-factor from that of a free electron can be thought of as a measure of the degree of spin-orbit coupling. The orbital magnetic moment need not be aligned with the electron spin magnetic moment, therefore this interaction is anticipated to be anisotropic and the g-factor is represented as a symmetric 2^{nk} rank tensor **g**. The **g**-tensor is diagonalized by rotation to the principal axis system, reducing it to the three principal values g_{xx}, g_{yy}, and g_{zz}. The Hamiltonian defining the energy of the Zeeman interaction is then, using matrix formalism,

$$\hat{H}_g = \beta_e \mathbf{S} \cdot \mathbf{g} \cdot \mathbf{H} \qquad [1.39]$$

As mentioned above, in nitroxides the unpaired electron is bound to an ^{14}N nucleus with nuclear spin angular momentum $I = 1$. In addition to influencing the g-factor, nuclei with non-zero spin values such as this will have an interaction with the electron spin called the hyperfine interaction, resulting in splitting of the EPR resonance absorption lines referred to as hyperfine splitting. In essence, the nuclear magnetic moment alters the local field at the electron, resulting in either an increase or decrease in the external field strength required to excite a transition. Recall that for an electron, there are two possible quantum states in the presence of an applied field, the +½ and –½ state, with the relative energies shown schematically in Figure 1.2. The nuclear magnetic moment can have three possible orientations corresponding to the $m_I = +1$, 0, and -1 states, and thus each spin state of the electron is split into three energy levels The selection rules of quantum mechanics dictate that $\Delta m_S = \pm 1$, $\Delta m_I = 0$, resulting in the three allowed transitions illustrated in Figure 1.5. In the $m_I = +1$ state, the nuclear magnetic moment increases the effective local field at the electron, such that for a given applied field the magnitude of the electron spin energies is increased. In the $m_I = -1$ state, the nuclear magnetic moment decreases the effective local field at the electron, such that for a given applied field the magnitude of the electron spin energies is decreased. The nuclear magnetic moment is zero for the $m_I = 0$ state and will not influence the energy of the electron spin states. In EPR, a constant frequency of microwave radiation is applied and the magnetic field is swept, and thus the applied field at which the resonance condition is met is shifted. In comparison to the resonant field for the $m_I = 0$ state, the field shift is up in the case of the $m_I = -1$ state and down in the case of the $m_I = +1$ state.

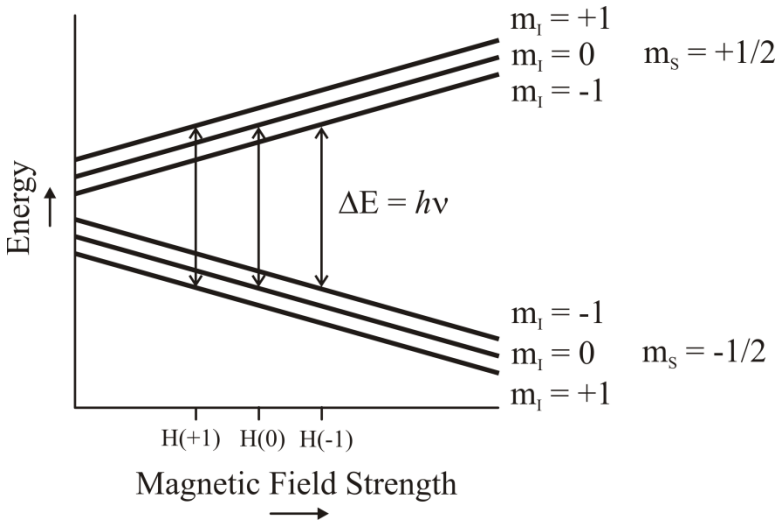

Figure 1.5 The resonance condition for an electron spin bound to a spin = 1 nucleus. The energy for each of the six states of the system is shown as a function of magnetic field strength. The three nuclear spin states result in three resonance lines, each corresponding to a transition between electron spin states stimulated when the indicated conditions for radiation frequency and magnetic field are met. The m_S and m_I values for each state are indicated on the right.

The hyperfine interaction has contributions from two sources: a dipolar interaction and Fermi contact interaction. The dipolar interaction between the nuclear and electron magnetic moments is a through space interaction with a Hamiltonian of the following form:

$$\widehat{H}_{A,dip} = g_0 \beta_e g_N \beta_N \left(\frac{\mathbf{I}\cdot\mathbf{S}}{r^3} - \frac{3(\mathbf{I}\cdot\mathbf{r})(\mathbf{S}\cdot\mathbf{r})}{r^5} \right) \quad [1.40]$$

where g_0 is the isotropic g-factor of the electron calculated by averaging the principal values of the **g**-tensor, g_N is the nuclear g-factor, β_N is the nuclear magneton, **I** is the nuclear angular momentum in units of $\hbar$, **r** is the interspin vector, and r is the distance between the electron and nucleus. The dot products of **I** and **S** with **r** are orientation-dependent, therefore the hyperfine interaction is anisotropic in non-spherical orbitals (e.g. p, d, f). The nitroxide nitrogen is sp^2 hybridized, and the unpaired electron occupies a 2p orbital highly localized to the nitrogen atom, giving it significant p_z character.

The Fermi contact interaction arises from direct electron contact with the nucleus, indicating that the electron has density at the nuclear center. Non-zero electron density at the

nucleus only occurs for s orbitals, therefore the electron has some sp^2 orbital occupancy. The Fermi contact interaction is isotropic and is represented with the Hamiltonian

$$\hat{H}_{A,Fermi} = a\mathbf{I} \cdot \mathbf{S} \quad [1.41]$$

where a is the isotropic hyperfine coupling constant

$$a = \frac{8\pi g_0 \beta_e g_N \beta_N}{3} |\psi(0)|^2 \quad [1.42]$$

In [1.42], $|\psi(0)|^2$ is the electron wavefunction probability density at the origin of the nucleus. The total hyperfine interaction can be represented using matrix notation using the following Hamiltonian:

$$\hat{H}_A = \mathbf{S} \cdot \mathbf{A} \cdot \mathbf{I} \quad [1.43]$$

A, like **g**, is a second rank tensor with the same principal axis sytem. **A** has principal values A_{xx}, A_{yy}, and A_{zz} and accounts for both the dipolar and Fermi contact interactions.

The polarity of the local environment is an additional factor that may influence the principal values of the **g** and **A** tensor (52). Although the electron primarily resides on the nitrogen atom in a 2p orbital, as mentioned above, it is somewhat delocalized along the NO bond, giving it some π-bond character. Spin labels at buried sites in globular proteins or along the transmembrane portion of membrane-bound proteins are in relatively apolar environments, causing electron delocalization along the NO bond to increase. Highly polar environments such as bulk water cause the electron density to become more concentrated to the nitrogen, increasing the density at the nitrogen nucleus and therefore increasing the isotropic hyperfine splitting and the g-factor deviation from the free electron value.

For nitroxides, ^{14}N provides the largest hyperfine splitting, but other nuclei on the nitroxide ring contribute to hyperfine structure. The twelve equivalent ^{1}H nuclei on the four methyl groups cause a splitting of ≈0.2 G, and the single ^{1}H on C4 of the ring causes a hyperfine

splitting of ≈0.5 G (53). This splitting is incredibly small compared to the ^{14}N hyperfine splitting, and is typically not observed in SDSL EPR due to any of a number of sources of linewidth broadening. One such source is a Heisenberg exchange contribution to T_2 relaxation caused by collision of the nitroxide with dissolved molecular oxygen. An investigation of oxygen Heisenberg exchange broadening found that at the physiological temperature of 37°C, an oxygen concentration of ≈0.18 mM is sufficient to broaden the nitroxide linewidth of the $m_I = 0$ nitrogen line to the point where the proton hyperfine structure is no longer resolved (54). The concentration of oxygen in water at room temperature is ≈0.3 mM (55), and the proton hyperfine interaction leads to a peak-to-peak linewidth of ≈1 G (in the absence of further broadening from other sources). Even in the absence of dissolved oxygen, the typical values used for microwave power and field modulation amplitude are sufficient to broaden out the proton hyperfine structure such that the proton hyperfine interaction leads to an observed broadening of linewidths rather than splitting of resonance lines.

Combination of [1.39] and [1.43] yields the Hamiltonian defining the resonance energy of the nitroxide, referred to as the Spin Hamiltonian.

$$\hat{H} = \beta_e \mathbf{S} \cdot \mathbf{g} \cdot \mathbf{H} + h\mathbf{S} \cdot \mathbf{A} \cdot \mathbf{I} \qquad [1.44]$$

This Hamiltonian is sufficient to explain spectra of a single nitroxide spin label attached to a protein, although a complete Hamiltonian for this system includes additional terms that are omitted in [1.44] (2). For example, a Zeeman term for the interaction of the nuclear spin with the external field is negligible because the magnetic field experienced by the nuclear spin due to the field created by the electron is much larger in magnitude than the externally applied field. The nuclear contribution to the Hamiltonian is dominated by the hyperfine interaction rather than the nuclear Zeeman interaction, therefore only the former is included in [1.44].

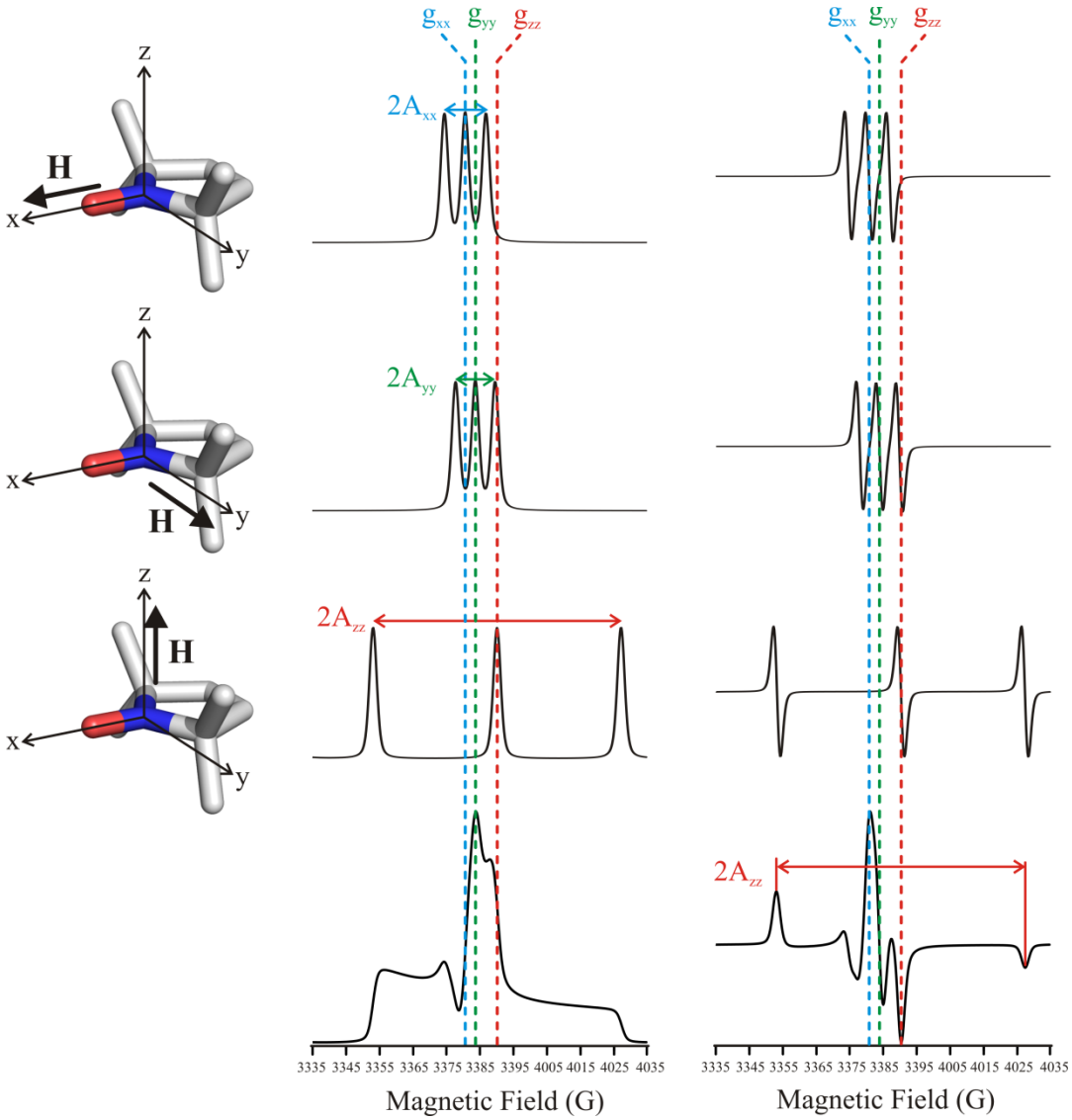

Figure 1.6 The rigid-limit spectrum of a nitroxide spin label. The absorption (center) and first-derivative (right) spectra of a single crystal doped with a nitroxide spin label reagent, where the crystal is oriented such that the external field **H** is aligned with the molecular principal axis system as indicated on the left. The molecular z-axis runs along the long axis of the nitrogen p orbital, the x-axis runs along the NO bond, the y-axis lies in the plane of the ring, perpendicular to x and z. If the crystal is crushed, the molecular orientations of the individual nitroxides are randomly distributed with respect to **H**, and the result is a powder spectrum shown at the bottom. The relationship of the principal A and g values to the spectral splitting and field position are indicated. Spectra were simulated at a frequency of 9.5 GHz using the principal values A_{xx} = 6.2 G, A_{yy} = 5.9 G, A_{zz} = 37 G, g_{xx} = 2.0078, g_{yy} = 2.0060, and g_{zz} = 2.0022.

As described above, both the Zeeman and hyperfine term in [1.44] are anisotropic, meaning the effective g-factor and hyperfine interaction energy depends on the relative orientation of the molecule with the external field. When the external field is aligned with one of

the three principal axes of the molecular frame, the principal values of the **g** and **A** tensors define the resonance position of the three hyperfine lines as shown in Figure 1.6. For the R1 side chain at solvent-exposed surface sites, the principal values A_{xx} = 6.2 G, A_{yy} = 5.9 G, A_{zz} = 37 G, g_{xx} = 2.0078, g_{yy} = 2.0060, and g_{zz} = 2.0022 were previously reported (56). The **g** tensor principal values determine the central field position, and the **A** values determine the splitting between the three resonance lines.

For an arbitrary orientation of the external field direction with respect to the molecular frame, defined by the polar and azimuthal angles θ and ϕ, the **g** and **A** tensors are reduced to the scalar values $g(\theta, \phi)$ and $A(\theta, \phi)$ and the resonance energy may be expressed as

$$\Delta E = h\nu = \beta_e g(\theta, \phi) H_{res} + hA(\theta, \phi) m_I \quad [1.45]$$

Rearranging [1.45] to solve for the magnetic field H_{res} yields

$$H_{res} = h\left(\frac{\nu - A(\theta,\phi) m_I}{\beta_e g(\theta,\phi)}\right) \quad [1.46]$$

which gives the three resonant field values for the three m_I values at a specific microwave frequency and orientation of the nitroxide. The EPR spectrum of a sample of nitroxides that are randomly oriented can be determined by a weighted sum over all angles. The spectrum thus calculated assumes a complete absence of motion.

In solution, the tumbling motion of the nitroxide results in an averaging of the anisotropy in the g-factor and hyperfine interaction (hereafter, together these are referred to as the magnetic anisotropies). The time scale of motion required to average the magnetic anisotropies can be understood in terms of a Bloch-McConnell multi-site exchange process (57-59). In this framework, states that give rise to distinct resonance positions exhibit broadening of the resonance line of each state and ultimately coalescence into a single resonance line as the rate of exchange increases. For the EPR spectrum of nitroxides, each orientation of the nitroxide with

respect to the external field corresponds to an individual state. Nitroxides with different orientations generate different resonance lines, as explained above, and exchange corresponds to reorientation resulting from molecular motion. The rate of motion required to average the different resonance lines such that they coalesce into a single line is approximately equal to the difference in the frequency of resonance, although other factors such as the intrinsic linewidth of each orientation and the relative populations in the absence of exchange also play a role. Thus, motional averaging of nitroxide magnetic anisotropies occurs with correlation times of

$$\tau \approx \frac{\hbar}{(A_{zz}-A_{xx})g_e\beta_e} \qquad [1.47]$$

and

$$\tau \approx \frac{\hbar}{(g_{xx}-g_{zz})\beta_e H} \qquad [1.48]$$

Inputting the principal A and g values given above for nitroxides attached to solvent-exposed sites on proteins, g_{xx}-g_{zz} ≈ 0.0056 and $A_{zz} - A_{xx}$ ≈ 31 G (9, 30), resulting in a correlation time of ≈6.9 ns and ≈1.8 ns, respectively. As correlation times become slower than the values given, the magnetic anisotropies are not averaged and the spectrum broadens, resulting in a spectrum approaching that given by a sum over [1.46] at sufficiently slow motion. As correlation times become faster than these values, the separate resonance lines for the different $g(\theta, \phi)$ and $A(\theta, \phi)$ merge and the spectrum exhibits three sharp resonance lines at positions given by the isotropic values of g and A: $\frac{1}{3}(g_{xx} + g_{yy} + g_{zz})$ and $\frac{1}{3}(A_{xx} + A_{yy} + A_{zz})$. It should be noted for the hyperfine anisotropy that complete motional averaging of the dipolar interaction results in zero splitting, but the Fermi contact interaction has no orientation-dependence and is therefore unaffected by molecular tumbling. Thus, the isotropic hyperfine splitting at very fast motions is due purely to Fermi contact.

The orientation-dependence of the EPR spectrum in combination with motional averaging is what gives it the structural and dynamical sensitivity discussed in the next section.

1.6 Lineshape analysis

The primary determinants of the CW EPR spectral lineshape for nitroxide-labeled proteins are anisotropy in the g-factor and hyperfine interaction (section **1.5**) and T_2 relaxation broadening (section **1.4**), both of which are sensitive to molecular motion. Internal spin label side chain motion as well as protein motion in the region local to the spin-labeled site contribute to the overall motion of the nitroxide; therefore local protein dynamics are encoded in the spectral lineshape. In this respect, CW EPR is a spectroscopy of motion, and a rigorous analysis of the spectral lineshape can provide quantitative information about the rate and angular amplitude (order) of nitroxide motion, as discussed below.

1.6.1 The intrinsic timescale of CW EPR. The time range typically specified as the region for sensitivity of the lineshape to molecular motion (specified in terms of correlation time) is 0.1-100 ns for X-band, because this is the timescale wherein motional contributions to T_2 relaxation broadening and averaging of magnetic anisotropies will significantly affect the spectral lineshape (Figure 1.7). The frequency difference of the anisotropies (splitting) determines the timescale of motion required to produce averaging of magnetic anisotropies (57-60), and since g-anisotropy is dependent on the microwave frequency, the time window for motional sensitivity of the lineshape can be shifted somewhat by operating at different EPR frequency bands.

When the motion is sufficiently fast to completely average out the magnetic anisotropies ($\tau < 0.1$ ns), referred to as the isotropic limit, the spectrum is becomes highly simplified to three sharp resonance lines of equivalent height and width. The resonance positions are specified by

the isotropic g-factor and hyperfine splitting values and may be calculated, for example, by the Breit-Rabi equation (1, 61-63). At the other end of the motional spectrum ($\tau > 100$ ns), the motion is too slow to produce averaging of magnetic anisotropy at X-band; this is referred to as the rigid limit. The spectral lineshape in this limit is relatively insensitive to motion and approaches that of a powder spectrum as correlation times approach infinity. Motional effects still contribute to T_2 relaxation until the true rigid limit (solid state) is reached, at which point T_2 relaxation contributions to the Lorentzian linewidth originate in solid-state spin-spin interactions such as proton (64, 65) and instantaneous diffusion (66). As such, there are small variations in lineshape in this motional regime due to differential T_2 broadening of homogeneous linewidths, but these are difficult to reliably measure experimentally. Proteins exhibit important functional motions on timescales slower than 100 ns. It is therefore important to be able to access motion on this timescale, which can be achieved using the EPR techniques of electron double resonance (17), saturation recovery (36), and saturation transfer spectroscopy (67-69).

1.6.2 Lineshape analysis in different motional regimes. Between the rigid and the isotropic limits ($\tau = 0.1 - 100$ ns), incomplete motional averaging of magnetic anisotropies and variation in T_2 relaxation broadening result in exquisite sensitivity of the spectral lineshape to both the rate and angular amplitude (order) of motion. In the fast motional regime ($\tau \approx 0.1 - 2$ ns), magnetic anisotropies are sufficiently averaged out such that three resonance lines are observed, similar to those predicted using the Breit-Rabi equation in the isotropic limit. However, the line heights and widths vary substantially for the different nuclear manifolds, indicating that the magnetic anisotropies are not fully averaged. Kivelson (70) and McConnell (6) developed expressions relating peak-to-peak linewidths and line heights to the rotational correlation time for isotropic motion, although the principal components of the **g** and **A** tensors

must be known (2, 71, 72). In the slow motional regime ($\tau \approx 10 - 100$ ns), Freed developed an empirical equation for determining the rotational correlation time from the effective A_{zz} splitting (A'_{zz}), which is the field separation of the low field peak and the high field trough (Figure 1.7) (49). These models provide quantitative measures of motion from directly measurable spectral quantities, but are unfortunately only applicable to a portion of the 0.1-100 ns time window and assume isotropic motion of the nitroxide, which is a limitation discussed next.

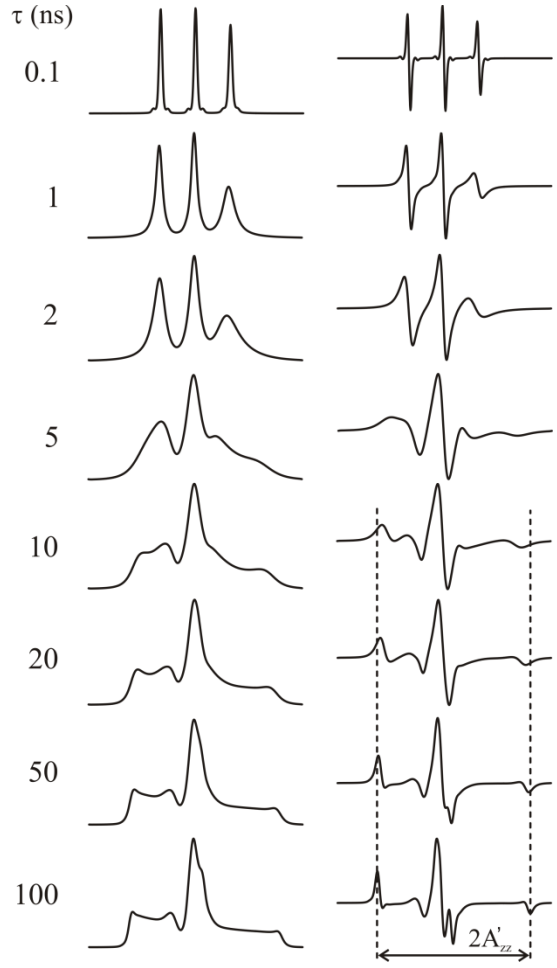

Figure 1.7 The effect of isotropic motion on the EPR spectral lineshape. Absorption (left) and first-derivative (right) spectra were simulated using the isotropic rotational correlation times indicated. The effective A_{zz} splitting (A'_{zz}) becomes resolved for τ longer than $\approx$10 ns. Spectra were simulated at a frequency of 9.5 GHz using the principal values A_{xx} = 6.2 G, A_{yy} = 5.9 G, A_{zz} = 37 G, g_{xx} = 2.0078, g_{yy} = 2.0060, and g_{zz} = 2.0022.

In the analyses of motional averaging discussed to this point, it is assumed that the nitroxide is tumbling isotropically in solution. However, in SDSL the nitroxide is covalently attached to a macromolecule, and the effective nitroxide τ is related to the correlation times for

protein rotary diffusion, local backbone fluctuations, and internal motion of the nitroxide side chain according to

$$\frac{1}{\tau} = \frac{1}{\tau_{\text{protein,rotary}}} + \frac{1}{\tau_{\text{protein,local}}} + \frac{1}{\tau_{\text{side chain}}} \qquad [1.49]$$

It is important to note that [1.49] is strictly valid only when the motional modes are independent and isotropic. According to [1.49], the rates (i.e. inverse correlation times) of the different motions are additive, and therefore the fastest motion will be the dominant factor in determining the spectral lineshape. For the CW EPR experiments reported in this dissertation, the contribution from protein rotary diffusion was minimized by the addition of the macroscopic viscogen Ficoll-70. This viscogen has negligible osmolytic effect (20) and therefore will not exert an osmotic pressure that may complicate the interpretation of high hydrostatic pressure effects that are the focus of this dissertation. The addition of the viscogen results in tumbling of the protein that is so slow that it can be approximated to be stationary, but does not influence internal motion of the spin label side chain (19, 20). The two important sources of motion are then rotameric motion of the spin label side chain and local backbone motion of the protein. Rotational motion from these sources is frequently restricted about the principal axes to differing degrees, resulting in differential averaging of the x, y, and z components of the magnetic anisotropies. In such cases, a more complex model is needed that can account for variations in both the rate and amplitude of motion. For the lineshape analysis presented in this dissertation, spectra are simulated according to a theoretical treatment of nitroxide motion developed by Freed and co-workers (29, 49) that can model isotropic and anisotropic motion across the entire relevant motional range of 0.1-100 ns.

1.6.3 The stochastic Liouville equation and microscopic order macroscopic disorder model. In the theory developed by Freed (49), the spectrum is calculated using a stochastic

Liouville equation (SLE), which is a semiclassical master diffusion equation in which the spins are treated quantum mechanically but the motional effects are treated as classical rotational diffusion. This approach allows calculation of spectra across the entire relevant motional range. The calculated spectrum is fit to the experimental one by least-squares minimization of the model parameters.

The microscopic order macroscopic disorder (MOMD) model is a motional model that may be implemented in simulations that use the SLE, and applies to spin-labeled lipid membranes and proteins. In this model, protein tumbling is assumed to be sufficiently slow that it is in the rigid limit, and the proteins are assumed to be randomly oriented with respect to the external field (macroscopic disorder). Tethering of the spin label to the protein results in restricted (anisotropic) motion of the label with respect to the protein (microscopic ordering). The parameters of primary importance in the determination of the spectral lineshape are discussed below, although a full description of all parameters in the MOMD model are discussed in detail in (29) for interested readers.

1.6.3.1 Coordinate frames. Three coordinate frames are typically employed in MOMD modeling of nitroxide motion (Figure 1.8). The magnetic frame (x_m, y_m, z_m) axes align with the principal axis system of the tensors **g** and **A**, which are coincident for R1 and its derivatives. This frame is fixed with respect to the structure of the nitroxide. The rotational diffusion frame (x_R, y_R, z_R) is principal axis system for the rotational diffusion tensor. Rotation about each axis is defined by an independent diffusion constant based on a Brownian model for rotation. The orientation of the three axes depends on the geometry of the label and its attachment to the protein backbone, and is generally not coincident with the magnetic frame. The diffusion frame

is related to the magnetic frame through the diffusion tilt angles α_D, β_D, and γ_D. As such, the diffusion frame is fixed with respect to the structure of the nitroxide.

The rotational diffusion axes will move as the nitroxide position fluctuates due to internal bond rotations of the R1 side chain and local protein backbone motion, but the attachment to the protein will generally result in partial ordering of this motion (anisotropy). For modeling motion of spin labels attached to proteins, this ordering is described with respect to a uniaxial director frame z_D, which is fixed with respect to the global protein structure. This is the only frame not fixed with respect to the nitroxide structure. z_D serves as the symmetry axis of the ordering potential employed in the MOMD model (see below) to constrain the extent of the spatial reorientation of the nitroxide.

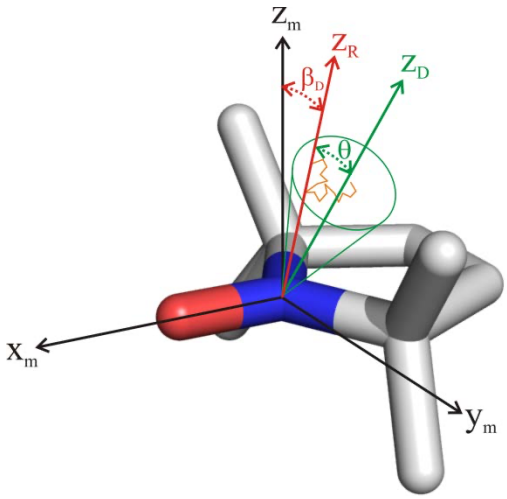

Figure 1.8 Principal frames employed in the MOMD model. The magnetic frame (x_m, y_m, z_m) is coincident with the molecular frame of the nitroxide. The z-axis of the diffusion frame (z_R) is fixed with respect to the magnetic frame at a position defined by the angle β_D. The uniaxial director frame (z_D) is fixed to the protein. z_R reorients with respect to z_D over time (orange line), and θ is the instantaneous angle between z_R and z_D. The average θ is used to calculate the order parameter S.

1.6.3.2 Magnetic parameters. These are the **g** and **A** tensor principal values (g_{xx}, g_{yy}, g_{zz}, A_{xx}, A_{yy}, A_{zz}) of the Spin Hamiltonian. They are typically determined experimentally using spectra of crystals at different orientations (73), fitting rigid limit spectra (56), or fitting spectra collected at multiple frequencies (74, 75). As mentioned in section **1.5**, local polarity can alter the **g** and **A** tensor values, so these values vary between solvent exposed surface sites and buried sites on globular proteins or transmembrane sites on membrane proteins. However, the values are

dictated primarily by the structure of the nitroxide ring and substituents, and typically are allowed to vary only slightly during fitting.

1.6.3.3 Rate. The rotational diffusion constants R_{xx}, R_{yy}, and R_{zz} define the rate of rotation about the principle axes of the diffusion frame x_R, y_R, and z_R, respectively. The values of these parameters are specified in the fitting program as $\log_{10}$ of the actual principal component values to make them the same order of magnitude as the non-dynamical fitting parameters. In the case of isotropic motion, these three constants will be equivalent and the x, y, and z components of the magnetic anisotropies will be averaged to the same degree (Figure 1.7). As discussed above, the nitroxide motion may be anisotropic, and in this case the values of R_{xx}, R_{yy}, and R_{zz} will not be the same and averaging of the x, y, and z components of the magnetic anisotropies will vary. An effective rotational correlation time can be calculated using

$$\tau = \frac{1}{6\times 10^{\overline{R}}} \qquad [1.50]$$

where $\overline{R}$ is the geometric mean of R_{xx}, R_{yy}, and R_{zz},

$$\overline{R} = \left(R_{xx}R_{yy}R_{zz}\right)^{1/3} \qquad [1.51]$$

In many cases spectra are well-characterized using an "axially symmetric" model for rotational diffusion, meaning rotation about two of the three principle diffusion axes is equivalent and slower than rotation about the third axis. The extreme case of this is shown in Figure 1.9 to illustrate what is commonly referred to as x-, y-, and z-anisotropy. To generate the spectra in this figure, the diffusion frame was taken to be equivalent to the magnetic frame ($\alpha_D = \beta_D = \gamma_D = 0$). Rotation about one axis is sufficiently fast to fully average the magnetic anisotropy of the other two, but rotation about the other two is sufficiently slow such that no averaging of the magnetic anisotropies occurs for the first axis (e.g. in Figure 1.9A, rotation about x is fast, and rotation about y and z is slow). Interestingly, the spectrum resulting from z-anisotropy is very similar to a

rigid limit spectrum (compare Figures 1.9C and 1.6). This illustrates the fact that averaging of x and y components of the magnetic anisotropies has little effect on the spectral lineshape, because the x and y magnetic parameter values are so similar. It is averaging of the x and y components with the z component of the magnetic anisotropies that leads to significant spectral changes.

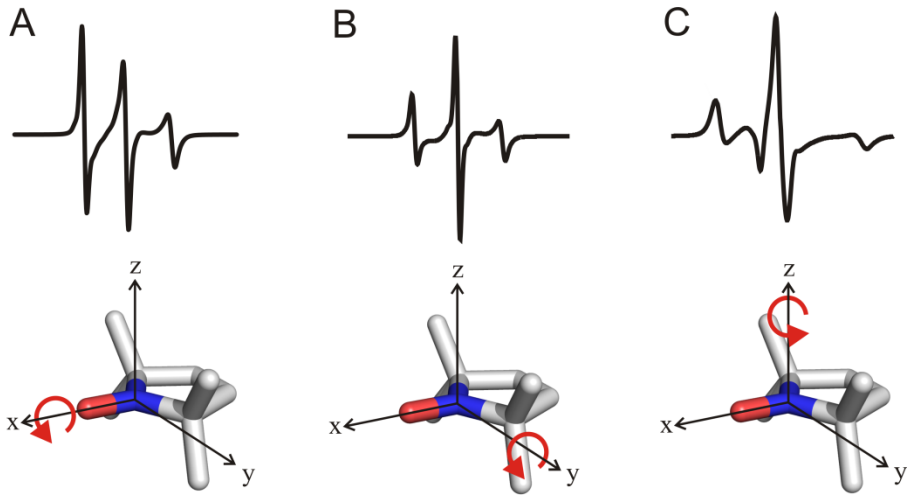

Figure 1.9 Principal axis anisotropies. Simulated spectra for rapid motion ($\tau = 0.1$ ns) about the (A) x-axis, (B) y-axis, and (C) z-axis of the molecular frame. To simulate the spectra, τ was set to 0.1 ns for the axis indicated by the red curved arrow, and 20 ns for the other two axes. A frequency of 9.5 GHz was used, and the principal magnetic values were $A_{xx} = 6.2$ G, $A_{yy} = 5.9$ G, $A_{zz} = 37$ G, $g_{xx} = 2.0078$, $g_{yy} = 2.0060$, and $g_{zz} = 2.0022$.

It should be noted that in this discussion of x-, y-, and z-anisotropy and in Figure 1.9, the diffusion tilt angles were taken to be zero, so that the diffusion frame and magnetic frame are coincident. Thus, the values of R_{xx}, R_{yy}, and R_{zz} correspond to rotational rates about the x, y, and z axes of the magnetic frame (x_m, y_m, z_m), respectively. However, non-zero values of these angles can rotate the diffusion frame to change how the magnetic parameters are mixed. For example, $\alpha_D = 0$, $\beta_D = 90^o$, $\gamma_D = 0$ causes rotation of the z_R axis to align it with x_m, resulting in averaging of z and y components of the magnetic anisotropies as a function of R_{zz}. $\alpha_D = 90^o$, $\beta_D = 90^o$, $\gamma_D = 0$ causes rotation of the z_R axis to align it with y_m, resulting in increased averaging of z and x components of the magnetic anisotropies as R_{zz} increases.

1.6.3.4 Order. The motional anisotropy associated with different rates of rotation about the principal axes of the diffusion frame was described above. An additional consideration is that the spin label will likely not freely rotate about each principal axis, due primarily to the attachment of the label to the protein. The restriction in the range of orientations of the spin label about one or more of these axes functions as an additional source of anisotropy. This restriction in motion is accounted for using a restoring (ordering) potential:

$$U(\Omega) = -kT \sum_{L,K} c_K^L D_{0K}^L(\Omega) \qquad [1.52]$$

The ordering potential $U(\Omega)$ is a function of the Euler angles relating the diffusion frame to the director frame, $D_{0K}^L(\Omega)$ are a restricted set of spherical harmonics, and the weighting coefficients c_K^L are the parameters fitted in the simulation. The uniaxial director frame z_D serves as the symmetry axis for the restoring potential, and the Euler angles Ω define the instantaneous position of the z_D axis with respect to the diffusion frame. There are five terms in this potential, although in most simulations only the first term is required to achieve a good fit. In this case, the potential becomes

$$U(\theta) = -\frac{1}{2} kT c_0^2 (3\cos^2\theta - 1) \qquad [1.53]$$

where θ is the angle between z_D and z_R. Expression [1.53] defines an energetic cost or gain as θ increases from 0^o to 90^o, depending on the sign and magnitude of the coefficient c_0^2. If c_0^2 is positive, the shape swept out by the z_D axis is approximately conical, where the size of the cone decreases as c_0^2 increases.

It is important to recall that the director frame is fixed with respect to the macromolecule, and therefore it will vary in position with respect to the nitroxide (i.e. the diffusion and magnetic frames). This description of a director frame that varies in position with respect to the diffusion frame is suggestive of a moving macromolecule and a static nitroxide, but an equivalent and

more appropriate perspective is to view the motion of the nitroxide with respect to a fixed macromolecule. In this perspective, the ordering potential describes the anisotropic distribution of nitroxide (diffusion frame) orientations with respect to the macromolecule (director frame), and the conical area swept out is that of the z_R axis with z_D serving as the center. The conical distribution of z_R axis orientations shown in Figure 1.8 is an illustration, and there is no rigid boundary for the possible orientations as a result of the ordering potential. This potential results in a probability distribution where the smaller θ angles are favored to an extent determined by the magnitude of c_0^2.

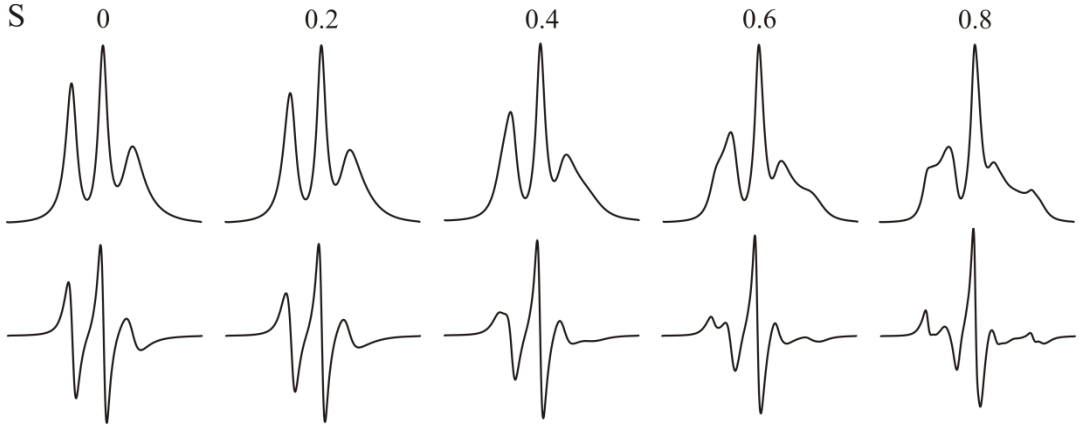

Figure 1.10 Order parameter dependence of the EPR spectral lineshape. Absorption (top) and first-derivative (bottom) spectra were simulated using the order parameter values indicated. An isotropic rotational correlation time of 2 ns and diffusion tilt angles $\alpha_D = 0$, $\beta_D = 36^o$, $\gamma_D = 0$ were used in all simulations. Spectra were simulated at a frequency of 9.5 GHz using the principal values $A_{xx} = 6.2$ G, $A_{yy} = 5.9$ G, $A_{zz} = 37$ G, $g_{xx} = 2.0078$, $g_{yy} = 2.0060$, and $g_{zz} = 2.0022$.

This ordering effect of the restoring potential is typically reported as an order parameter (S) defined as

$$S = \frac{1}{2}\langle(3\cos^2\theta - 1)\rangle \qquad [1.54]$$

where the brackets indicate a spatial average. The spectral lineshape dependence on S is illustrated in Figure 1.10. It should be noted that the order parameter denoted by S is unrelated to the spin angular momentum **S** discussed earlier in this chapter. In a few cases in this dissertation,

a second term for the restoring potential, with L=K=2, was used in spectral simulations. In these cases, c_0^2 and c_2^2 were positive, and the effect of the second term on the shape of the potential was the elongate the cone along one axis to generate an elliptic cone.

1.6.4 Limitations of spectral simulation with the SLE. It is important to emphasize that although spectral simulations are an important analytical tool for determining motional information from spectral lineshapes, there are practical issues that limit the application of this approach. The primary issue is that the SLE simulations use a large number of parameters that are often correlated, leading to the possibility of more than one equally-good fit (i.e. degeneracy of the fits). Additionally, simulations are generally time-consuming and are therefore not ideal for analyzing large datasets. These problems are compounded in the case of conformational exchange that generates a multicomponent spectrum, because the number of parameters is increased and the components are not fully resolved (at X-band).

1.7 Double electron-electron resonance (DEER)

The addition of a second spin label into the protein introduces the possibility for measuring distances between them *via* the dipolar interaction, which is proportional to $1/r^3$, where r is the interspin distance. When the two spin labels are close ($\lesssim 30$ Å), the dipolar interaction reduces the T_2 relaxation time sufficiently to determine the interspin distance based on broadening of the EPR spectrum (76, 77). Alternatively, saturation recovery can measure T_1 relaxation-enhancement to determine distances between spins (78). CW EPR and relaxation-based measurements have the advantage that they can be measured at room temperature, whereas DEER currently requires cryogenic temperatures (see below). The disadvantage to the CW and relaxation enhancement methods is that they are limited to shorter distances for spin-labeled proteins (≈30 Å for CW, ≈40 Å for relaxation at room temperature), and in the case of relaxation,

provide only an average distance and not a distribution. Due to these limitations, DEER is by far the most commonly used technique for measuring interspin distance distributions (79) and is employed in this dissertation. DEER is an increasingly popular technique (79, 80) that can measure distances in the range of ≈20-80 Å. The principal advantage of DEER is that it provides the full distribution of interspin distances including their relative probability. For a doubly-labeled protein, the discrete distances report each structural state in the ensemble, and the widths indicate the heterogeneity of each state. In this manner, DEER measures structure and structural heterogeneity of the conformational ensemble. Double quantum coherence is an alternative pulsed experiment that can measure distance distributions comparable to DEER (81-83), but current commercially-available instrumentation is better suited to DEER. This section provides an overview of the basic principles of the DEER experiment; more detailed descriptions of the theory and practical implementation of DEER are available elsewhere (84-87).

1.7.1 Hamiltonian for the electron-electron dipolar interaction. The additional electron spin requires modification of the Spin Hamiltonian described in section **1.5**. In the high field limit, this interaction is small compared to the Zeeman interaction and may therefore be treated using perturbation theory as a separate, additive term to the Spin Hamiltonian. This term, for two free electron spins A and B, may be represented analogously to the hyperfine dipolar interaction expression ([1.40]) as follows:

$$\widehat{H}_{dd} = c\frac{1}{r_{AB}^3}\left[\mathbf{S}_A \cdot \mathbf{S}_B - \frac{3}{r_{AB}^2}(\mathbf{S}_A \cdot \mathbf{r}_{AB})(\mathbf{S}_B \cdot \mathbf{r}_{AB})\right] \quad [1.55]$$

where r_{AB} is the distance between the two spins, $\mathbf{r}$ is the interspin vector, $\mathbf{S}_A$ and $\mathbf{S}_B$ are the spin angular momenta vector operators, and

$$c = \frac{\mu_0}{4\pi\hbar} g_A g_B \beta_e^2 \quad [1.56]$$

where μ_0 is the vacuum permeability, and g_A and g_B are the isotropic g-factors for each spin. The dipolar interaction Hamiltonian term can be expanded into six terms, and all but one are negligible in the high field limit and when the difference in resonant frequency between the two spins is greater than the dipolar frequency (1, 83), leaving

$$\hat{H}_{dd} = c\frac{1}{r_{AB}^3}(3\cos^2\theta - 1)S_{z,A}S_{z,B} \quad [1.57]$$

where θ is the angle between the interspin vector and the external field. The dipolar coupling frequency is given by $\omega_{AB} = c\frac{1}{r_{AB}^3}(3\cos^2\theta - 1)$. The fundamental aim of the DEER measurement is to isolate and measure the dipolar coupling frequency ω_{AB} to determine r_{AB}.

1.7.2 DEER pulse sequence and signal. Different pulse sequences may be used for the DEER experiment, including a 3-pulse (87), 4-pulse (86), and 5-pulse sequence (88); the 4-pulse sequence shown in Figure 1.11 was used in all DEER experiments reported in this dissertation. In 4-pulse DEER, a refocused primary echo pulse sequence (i.e. observe sequence) is used to populate an echo for a subset of spins in the sample (i.e. observe spins or A spins). Using the bulk magnetization framework of Bloch (section **1.4**), the $\pi/2$ pulse along the x-axis aligns the bulk magnetization vector along the negative y-axis, and afterwards the individual spins precess about the z-axis at slightly different frequencies due to local field inhomogeneities in the sample, causing a loss of magnetization in the xy-plane. The initial π pulse of the observe sequence inverts the precession direction, and the magnetization will realign in the xy-plane at a time τ_1 after the π pulse equal to the separation of the $\pi/2$ and π pulses, forming the primary echo. After another fixed time interval τ_2, a second π pulse inverts the precession direction again, resulting in a secondary (i.e. refocused) echo at a time τ_2 after the second π pulse. The intensity of this echo, V, is the signal measured in the DEER experiment.

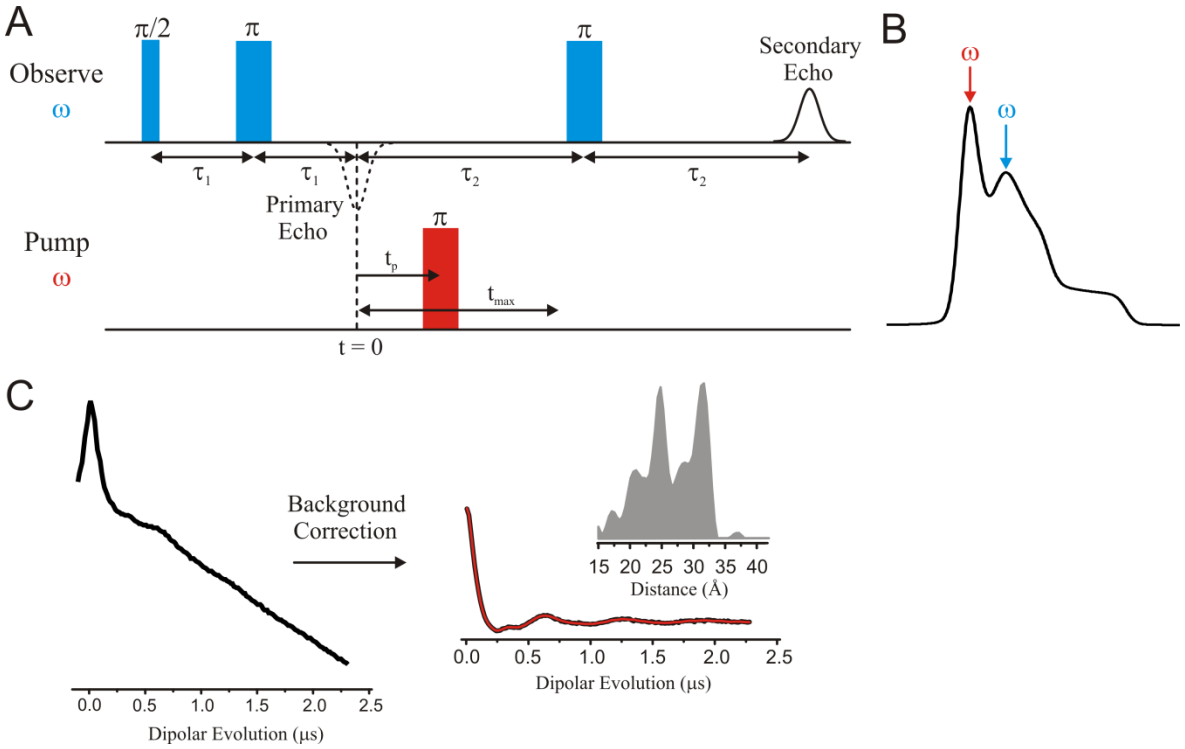

Figure 1.11 The DEER experiment. (A) The four-pulse DEER sequence described in the text employs pulses of microwave radiation at two different frequencies (blue and red) to induce transitions in two different populations of spins. (B) The angular frequencies ω for the observe (blue) and pump (red) sequence correspond to different positions in the spectral lineshape, thus exciting separate spin populations. The absorption spectrum shown is a simulated rigid limit spectrum of a nitroxide at 33.5 GHz (Q-band), which is the frequency employed for DEER experiments reported in this dissertation. (C) The raw DEER data shown on the left is background-corrected to remove the intermolecular contribution to the signal, and the intramolecular form factor is then fit (red trace) to determine the distance distribution (in grey) for the spin pair.

In the time between the first and second observe π pulses, an inversion of magnetization for a second population of spins (i.e. pump spins or B spins) is triggered using a π pulse at a different frequency (i.e. pump frequency). This changes the local field at the observe spins, which introduces a phase gain of $\omega_{AB}t_p$ to these spins, where the time t_p gives the pump pulse position with respect to the primary echo position and ω_{AB} is the dipolar coupling frequency described in section **1.7.1**. The pump pulse position is varied, modulating V with a period equal to $1/\omega_{AB}$; therefore $V(t_p)$ is proportional to $\cos(\omega_{AB}t_p)$.

It should be noted that, even in the absence of the pump pulse, the echo intensity V decays exponentially as a function of the pulse separation times τ_1 and τ_2,

$$V \propto exp\left[-\left(\frac{1}{T_2} + k_{ID,A}\right)(\tau_1 + \tau_2)\right] \quad [1.58]$$

where the decay rate constant is proportional to the instantaneous diffusion rate $k_{ID,A}$ and inversely proportional to the spin-spin relaxation time T_2 (66). The instantaneous diffusion rate $k_{ID,A}$ is proportional to the concentration of A spins, therefore the signal loss will occur as sample concentration increases. The pulse separation times are critical parameters in the DEER experiment, because they determine the maximum t_p for which data may be collected (t_{max}) (Figure 1.11). The time domain over which V is measured must be sufficiently long that the oscillation period and thus ω_{AB} may be accurately determined. The maximum reliable distance $r_{max,\langle r\rangle}$ that may be determined is

$$r_{max,\langle r\rangle} \approx 5\sqrt[3]{t_{max}/2\mu s} \quad [1.59]$$

The maximum distance for which the width of the distribution is reliable, $r_{max,\langle\sigma\rangle}$, is

$$r_{max,\langle\sigma\rangle} \approx 4\sqrt[3]{t_{max}/2\mu s} \quad [1.60]$$

Thus, a t_{max} of ≈6.5 μs is required for reliable distances and widths to be determined to 60 Å. For nitroxides, T_2 is prohibitively short at room temperature (≈10-30 ns), therefore samples are cooled to cryogenic temperatures to lengthen relaxation times. In addition to freezing, buffer deuteration can further lengthen T_2 to allow access to longer distances (89). Freezing samples serves a second purpose, namely to avoid molecular tumbling that would result in motional averaging of the dipolar interaction as described in section **1.5**.

In the frozen sample, the interspin vectors are randomly distributed in terms of orientation with respect to the external field, defined by θ in [1.57]. The relative population for each angle follows a sin(θ) distribution, indicating that perpendicular orientations are more likely than parallel orientations. Assuming equivalent excitation of each orientation, a distribution of

dipolar frequencies will be observed for a particular interspin distance, representative of the different angles of the interspin vectors. The DEER signal $V(t_p)$ for a spin pair at a fixed distance, but with random orientation with respect to the external field, can be analytically calculated by integrating over all possible θ angles (90)

$$V(t_p) = 1 - \lambda + \lambda \int_0^{\pi/2} \xi(\theta) \cos(\omega_{AB} t_p) \sin(\theta) d\theta \quad [1.61]$$

where the modulation depth λ reflects the fraction of spins coupled to A spins that are inverted by the pump pulse and $\xi(\theta)$ is an excitation function that defines the relative excitation as a function of the interspin vector orientation; $\xi(\theta)$ is ≈1 for nitroxides. Expression [1.61] ignores any contribution from orientation selection, which refers to the dependence of the dipolar frequency on the relative orientation of the molecular frames of the two spin labels (91). Orientation selection effects arise for rigidly oriented samples where the excitation coverage is incomplete across all θ values, but are rarely observed for nitroxide-labeled proteins due to the inherent flexibility of both the protein and the spin label side chain (79).

Up to this point, the DEER signal has been described for two spins in a protein with a fixed distance between them. In reality, the flexibility of proteins results in a distribution of distances, and calculation of the DEER signal requires summation over all interspin distances weighted by their probabilities:

$$V(t_p) = \left[1 - \lambda + \lambda \int_{r_{min}}^{r_{max}} \int_0^{\pi/2} \xi(\theta) \cos(\omega_{AB} t_p) P(r) \sin(\theta) d\theta dr\right] B(t_p) \quad [1.62]$$

where P(r) is the distance distribution function and $B(t_p)$ is the background function describing the echo attenuation due to interactions between spins on different proteins. The intermolecular interaction contribution to the echo intensity has the form

$$B(t_p) = exp\left[k_{ID,B} t_p^{D/3}\right] \quad [1.63]$$

where $k_{ID,B}$ is the instantaneous diffusion rate for B spins and D is the fractional dimension, or dimensionality (92). For a random distribution of globular proteins in solution D is expected to be ≈3, and for membrane proteins in a bilayer D is expected to be ≈2. The background may be determined experimentally using singly-labeled mutants where the intramolecular interaction is eliminated, and it is apparent from experiments of this kind that the observed $B(t_p)$ may have non-ideal values of D (93). Typically, $B(t_p)$ is fitted using the raw DEER data of the doubly-labeled mutant under investigation.

To solve for the distance distribution function, the background is removed and the remaining time domain data (referred to as the dipolar evolution function or form factor) is discretized and converted into a system of linear algebraic functions of the form:

$$\mathbf{F}(t_p) = \mathbf{K}(r, t_p) \cdot \mathbf{P}(r) \qquad [1.64]$$

F is a vector containing the background-corrected data, **P** is the probability distribution, and **K** is a kernel function that is equivalent to the integral [1.61]. For a given **P**, a kernel function may be readily constructed to solve for **F**. However, the inverse problem of solving for a **P** which fits a given **F** is ill-posed (94). Tikhonov regularization is the most commonly employed method for solving this equation for the distance distribution **P** and has been implemented in DEERAnalysis (95), a Matlab-based software package that may be downloaded at: http://www.epr.ethz.ch/software. Alternative methods have been employed for the analysis of DEER data, including a maximum entropy modification to suppress negative probabilities in the distance distribution function (96). In this dissertation, all DEER data were analyzed using the program LongDistances, which employs a modified regression analysis. This program was written by Dr. Christian Altenbach in LabVIEW and is available online at: http://www.biochemistry.ucla.edu/biochem/Faculty/Hubbell/.

1.8 References

1. Abragam A (1961) *The Principles of Nuclear Magnetism* (University Press, Oxford).
2. Poole J, Charles P. (1983) *Electron Spin Resonance: A Comprehensive Treatise on Experimental Techniques* (John Wiley & Sons, Inc., USA).
3. Slichter CP (1963) *Principles of Magnetic Resonance, with Examples from Solid State Physics* (Harper & Row, New York).
4. Carrington A & McLachlan AD (1967) *Introduction to Magnetic Resonance with Applications to Chemistry and Chemical Physics* (Harper & Row, New York,).
5. Burr M & Koshland DE, Jr. (1964) Use of "reporter groups" in structure-function studies of proteins. *Proc Natl Acad Sci USA* 52:1017-1024.
6. Stone TJ, Buckman T, Nordio PL, & McConnell HM (1965) Spin-labeled biomolecules. *Proc Natl Acad Sci USA* 54(4):1010-1017.
7. Mchaourab HS, Lietzow MA, Hideg K, & Hubbell WL (1996) Motion of spin-labeled side chains in T4 Lysozyme. Correlation with protein structure and dynamics. *Biochemistry* 35(24):7692-7704.
8. Mchaourab HS, Kálai T, Hideg K, & Hubbell WL (1999) Motion of spin-labeled side chains in T4 Lysozyme: effect of side chain structure. *Biochemistry* 38(10):2947-2955.
9. Columbus L, Kálai T, Jekö J, Hideg K, & Hubbell WL (2001) Molecular motion of spin labeled side chains in α-helices: analysis by variation of side chain structure. *Biochemistry* 40(13):3828-3846.
10. Hubbell WL, López CJ, Altenbach C, & Yang Z (2013) Technological advances in site-directed spin labeling of proteins. *Curr Opin Struct Biol* 23(5):725-733.

11. Campbell ID & Dwek RA (1984) *Biological Spectroscopy* (Benjamin-Cummings Publishing Co., Menlo Park, CA).

12. Dupeyre R-M & Rassa A (1966) Nitroxides. XIX. Norpseudopelletierine-N-oxyl, a new, stable, unhindered free radical. *J Am Chem Soc* 88(13):3180-3181.

13. Getz EB, Xiao M, Chakrabarty T, Cooke R, & Selvin PR (1999) A comparison between the sulfhydryl reductants tris(2-carboxyethyl)phosphine and dithiothreitol for use in protein biochemistry. *Anal Biochem* 273(1):73-80.

14. Todd AP, Cong J, Levinthal F, Levinthal C, & Hubbell WL (1989) Site-directed mutagenesis of colicin E1 provides specific attachment sites for spin labels whose spectra are sensitive to local conformation. *Proteins: Struct, Funct, Bioinf* 6(3):294-305.

15. Fleissner MR, Cascio D, & Hubbell WL (2009) Structural origin of weakly ordered nitroxide motion in spin-labeled proteins. *Protein Sci* 18(5):893-908.

16. Warshaviak DT, Serbulea L, Houk KN, & Hubbell WL (2011) Conformational analysis of a nitroxide side chain in an α-helix with density functional theory. *J Phys Chem B* 115(2):397-405.

17. Fleissner MR*, et al.* (2011) Structure and dynamics of a conformationally constrained nitroxide side chain and applications in EPR spectroscopy. *Proc Natl Acad Sci USA* 108(39):16241-16246.

18. Schmidt MJ, Borbas J, Drescher M, & Summerer D (2014) A genetically encoded spin label for electron paramagnetic resonance distance measurements. *J Am Chem Soc* 136(4):1238-1241.

19. López CJ, Fleissner MR, Brooks EK, & Hubbell WL (2014) Stationary-phase EPR for exploring protein structure, conformation, and dynamics in spin-labeled proteins. *Biochemistry* 53(45):7067-7075.

20. López CJ, Fleissner MR, Guo Z, Kusnetzow AK, & Hubbell WL (2009) Osmolyte perturbation reveals conformational equilibria in spin-labeled proteins. *Protein Sci* 18(8):1637-1652.

21. Lillington JED*, et al.* (2011) Shigella flexneri Spa15 crystal structure verified in solution by double electron electron resonance. *J Mol Biol* 405(2):427-435.

22. Gruene T*, et al.* (2011) Integrated analysis of the conformation of a protein-linked spin label by crystallography, EPR and NMR spectroscopy. *J Biomol NMR* 49(2):111-119.

23. Raghuraman H*, et al.* (2012) Mechanism of Cd^{2+} coordination during slow inactivation in potassium channels. *Structure* 20(8):1332-1342.

24. Kroncke BM, Horanyi PS, & Columbus L (2010) Structural origins of nitroxide side chain dynamics on membrane protein α-helical sites. *Biochemistry* 49(47):10045-10060.

25. Fraser RR, Boussard G, Saunders JK, Lambert JB, & Mixan CE (1971) Barriers to rotation about the sulfur-sulfur bond in acyclic disulfides. *J Am Chem Soc* 93(15):3822-3823.

26. Cunningham TF*, et al.* (2012) High-resolution structure of a protein spin-label in a solvent-exposed β-sheet and comparison with DEER spectroscopy. *Biochemistry* 51(32):6350-6359.

27. Freed DM, Khan AK, Horanyi PS, & Cafiso DS (2011) Molecular origin of electron paramagnetic resonance line shapes on β-barrel membrane proteins: the local solvation environment modulates spin-label configuration. *Biochemistry* 50(41):8792-8803.

28. Bracken C, Carr PA, Cavanagh J, & Palmer III AG (1999) Temperature dependence of intramolecular dynamics of the basic leucine zipper of GCN4: implications for the entropy of association with DNA1. *J Mol Biol* 285(5):2133-2146.

29. Budil DE, Lee S, Saxena S, & Freed JH (1996) Nonlinear-least-squares analysis of slow-motion EPR spectra in one and two dimensions using a modified Levenberg–Marquardt algorithm. *J Magn Reson, Ser A* 120(2):155-189.

30. Columbus L & Hubbell WL (2004) Mapping backbone dynamics in solution with site-directed spin labeling: GCN4−58 bZip free and bound to DNA. *Biochemistry* 43(23):7273-7287.

31. Isas JM, Langen R, Haigler HT, & Hubbell WL (2002) Structure and dynamics of a helical hairpin and loop region in annexin 12: a site-directed spin labeling study. *Biochemistry* 41(5):1464-1473.

32. López CJ, Oga S, & Hubbell WL (2012) Mapping molecular flexibility of proteins with site directed spin labeling: a case study of myoglobin. *Biochemistry* 51(33):6568-6583.

33. López CJ, Yang Z, Altenbach C, & Hubbell WL (2013) Conformational selection and adaptation to ligand binding in T4 lysozyme cavity mutants. *Proc Natl Acad Sci USA* 110(46):E4306-E4315.

34. Humphries GMK & McConnell HM (1982) Nitroxide spin labels. *Methods in Experimental Physics*, eds Gerald E & Harold L (Academic Press), Vol 20, pp 53-122.

35. Bloch F (1946) Nuclear induction. *Phys Rev* 70(7-8):460-474.

36. Bridges MD, Hideg K, & Hubbell WL (2010) Resolving conformational and rotameric exchange in spin-labeled proteins using saturation recovery EPR. *Appl Magn Reson* 37(1-4):363-363.

37. Sato H*, et al.* (2008) Electron spin–lattice relaxation of nitroxyl radicals in temperature ranges that span glassy solutions to low-viscosity liquids. *J Magn Reson* 191(1):66-77.

38. Robinson BH, Haas DA, & Mailer C (1994) Molecular dynamics in liquids: spin-lattice relaxation of nitroxide spin labels. *Science* 263(5146):490-493.

39. Eaton S & Eaton G (2002) Relaxation times of organic radicals and transition metal ions. *Distance Measurements in Biological Systems by EPR,* Biological Magnetic Resonance, eds Berliner L, Eaton G, & Eaton S (Springer, US), Vol 19, pp 29-154.

40. Owenius R, Terry GE, Williams MJ, Eaton SS, & Eaton GR (2004) Frequency dependence of electron spin relaxation of nitroxyl radicals in fluid solution. *J Phys Chem B* 108(27):9475-9481.

41. Sato H*, et al.* (2008) Impact of electron−electron spin interaction on electron spin relaxation of nitroxide diradicals and tetraradical in glassy solvents between 10 and 300 K. *J Phys Chem B* 112(10):2818-2828.

42. Griffiths DJ (2005) *Introduction to quantum mechanics* (Pearson Prentice Hall, Upper Saddle River, NJ) 2nd edition.

43. Atkins PW & Kivelson D (1966) ESR linewidths in solution. II. Analysis of spin—rotational relaxation data. *J Chem Phys* 44(1):169-174.

44. Eaton G & Eaton S (1989) Resolved electron-electron spin-spin splittings in EPR spectra. *Spin Labeling,* Biological Magnetic Resonance, eds Berliner L & Reuben J (Springer US), Vol 8, pp 339-397.

45. Redfield AG (1957) On the theory of relaxation processes. *IBM J Res Dev* 1(1):19-31.

46. Redfield AG (1965) The theory of relaxation processes. *Advances in Magnetic and Optical Resonance*, ed John SW (Academic Press), Vol 1, pp 1-32.

47. Millhauser GL & Freed JH (1984) Two-dimensional electron spin echo spectroscopy and slow motions. *J Chem Phys* 81(1):37-48.

48. Stillman AE, Schwartz LJ, & Freed JH (1980) Direct determination of rotational correlation time by electron-spin echoes. *J Chem Phys* 73(7):3502-3503.

49. Freed JH (1976) Theory of slow tumbling ESR spectra for nitroxides. *Spin Labeling Theory and Applications*, ed Berliner LJ (Academic Press, New York, NY), pp 53-132.

50. Altenbach C, Froncisz W, Hyde JS, & Hubbell WL (1989) Conformation of spin-labeled melittin at membrane surfaces investigated by pulse saturation recovery and continuous wave power saturation electron paramagnetic resonance. *Biophys J* 56(6):1183-1191.

51. Likhtenshtein GI, Yamauchi J, Nakatsuji Si, Smirnov AI, & Tamura R (2008) Fundamentals of magnetism. *Nitroxides* (Wiley-VCH Verlag GmbH & Co. KGaA), pp 1-45.

52. Shimshick EJ & McConnell HM (1973) Lateral phase separation in phospholipid membranes. *Biochemistry* 12(12):2351-2360.

53. Robinson BH, Mailer C, & Reese AW (1999) Linewidth analysis of spin labels in liquids: I. Theory and data analysis. *J Magn Reson* 138(2):199-209.

54. Hyde JS & Subczynski WK (1984) Simulation of ESR spectra of the oxygen-sensitive spin-label probe CTPO. *J Magn Reson* 56(1):125-130.

55. Wilhelm E, Battino R, & Wilcock RJ (1977) Low-pressure solubility of gases in liquid water. *Chem Rev* 77(2):219-262.

56. Kusnetzow AK, Altenbach C, & Hubbell WL (2006) Conformational states and dynamics of rhodopsin in micelles and bilayers. *Biochemistry* 45(17):5538-5550.

57. McConnell HM (1958) Reaction rates by nuclear magnetic resonance. *J Chem Phys* 28(3):430-431.

58. Abergel D & Palmer AG (2004) Approximate solutions of the Bloch–McConnell equations for two-site chemical exchange. *ChemPhysChem* 5(6):787-793.

59. Palmer III AG (2004) NMR characterization of the dynamics of biomacromolecules. *Chem Rev* 104(8):3623-3640.

60. Marsh D (1989) Experimental methods in spin-label spectral analysis. *Spin Labeling Theory and Applications,* Biological Magnetic Resonance, eds Berliner L & Reuben J (Springer, US), Vol 8, pp 255-303.

61. Weil JA (1971) The analysis of large hyperfine splitting in paramagnetic resonance spectroscopy. *J Magn Reson* 4(3):394-399.

62. Stoll S & Schweiger A (2007) Easyspin: simulating CW ESR spectra. *Biol Magn Reson* 27:299-321.

63. Breit G & Rabi II (1931) Measurement of nuclear spin. *Phys Rev* 38(11):2082-2083.

64. Bloembergen N (1949) On the interaction of nuclear spins in a crystalline lattice. *Physica* 15(3–4):386-426.

65. Kevan L & Schwartz RN (1979) *Time domain electron spin resonance* (Wiley, New York).

66. Schweiger A & Jeschke G (2001) *Principles of pulse electron paramagnetic resonance* (Oxford University Press, Oxford, UK; New York).

67. Hyde JS (1978) Saturation-transfer spectroscopy. *Enzyme Structure, Part G*, Methods in Enzymology, eds Hirs CHW & Timasheff SN (Academic Press), Vol 49, pp 480-511.

68. Thomas DD (1978) Large-scale rotational motions of proteins detected by electron paramagnetic resonance and fluorescence. *Biophys J* 24(2):439-462.

69. Dalton LR, Robinson BH, Dalton LA, & Coffey P (1976) Saturation transfer spectroscopy. *Advances in Magnetic and Optical Resonance*, ed Waugh JS (Academic Press), Vol 8, pp 149-259.

70. Kivelson D (1960) Theory of ESR linewidths of free radicals. *J Chem Phys* 33(4):1094-1106.

71. Schreier S, Polnaszek CF, & Smith ICP (1978) Spin labels in membranes problems in practice. *Biochim Biophys Acta, Rev Biomembr* 515(4):395-436.

72. Knowles PF, Marsh D, & Rattle HWE (1976) *Magnetic resonance of biomolecules: an introduction to the theory and practice of NMR and ESR in biological systems* (Wiley, London; New York).

73. Griffith OH, Cornell DW, & McConnell HM (1965) Nitrogen hyperfine tensor and g tensor of nitroxide radicals. *J Chem Phys* 43(8):2909-2910.

74. Liang Z, Lou Y, Freed JH, Columbus L, & Hubbell WL (2004) A multifrequency electron spin resonance study of T4 lysozyme dynamics using the slowly relaxing local structure model. *J Phys Chem B* 108(45):17649-17659.

75. Barnes JP, Liang Z, Mchaourab HS, Freed JH, & Hubbell WL (1999) A multifrequency electron spin resonance study of T4 lysozyme dynamics. *Biophys J* 76(6):3298-3306.

76. Altenbach C, Oh K-J, Trabanino RJ, Hideg K, & Hubbell WL (2001) Estimation of inter-residue distances in spin labeled proteins at physiological temperatures: experimental strategies and practical limitations. *Biochemistry* 40(51):15471-15482.

77. Kittell AW, Hustedt EJ, & Hyde JS (2012) Inter-spin distance determination using L-band (1-2 GHz) non-adiabatic rapid sweep electron paramagnetic resonance (NARS EPR). *J Magn Reson* 221:51-56.

78. Yang Z*, et al.* (2014) Long-range distance measurements in proteins at physiological temperatures using saturation recovery EPR spectroscopy. *J Amer Chem Soc* 136(43):15356-15365.

79. Jeschke G (2012) DEER distance measurements on proteins. *Ann Rev Phys Chem* 63(1):419-446.

80. Mchaourab Hassane S, Steed PR, & Kazmier K (2011) Toward the fourth dimension of membrane protein structure: insight into dynamics from spin-labeling EPR spectroscopy. *Structure* 19(11):1549-1561.

81. Borbat PP & Freed JH (1999) Multiple-quantum ESR and distance measurements. *Chem Phys Lett* 313(1–2):145-154.

82. Borbat PP & Freed JH (2000) Double-quantum ESR and distanct measurements. *Distance measurements in biological systems by EPR*, Biological Magnetic Resonance, (Academic/Plenum, New York), Vol 19, pp 385-459.

83. Borbat PP & Freed JH (2013) Pulse dipolar electron spin resonance: distance measurements. *Structural Information from Spin-Labels and Intrinsic Paramagnetic Centres in the Biosciences,* Structure and Bonding, eds Timmel CR & Harmer JR (Springer Berlin Heidelberg), Vol 152, pp 1-82.

84. Jeschke G, Panek G, Godt A, Bender A, & Paulsen H (2004) Data analysis procedures for pulse ELDOR measurements of broad distance distributions. *Appl Magn Reson* 26(1-2):223-244.

85. Salikhov KM, Dzuba SA, & Raitsimring AM (1981) The theory of electron spin-echo signal decay resulting from dipole-dipole interactions between paramagnetic centers in solids. *J Magn Reson* 42(2):255-276.

86. Pannier M, Veit S, Godt A, Jeschke G, & Spiess HW (2000) Dead-time free measurement of dipole-dipole interactions between electron spins. *J Magn Reson* 142(2):331-340.

87. Milov AD, Ponomarev AB, & Tsvetkov YD (1984) Electron-electron double resonance in electron spin echo: model biradical systems and the sensitized photolysis of decalin. *Chem Phys Lett* 110(1):67-72.

88. Borbat PP, Georgieva ER, & Freed JH (2012) Improved sensitivity for long-distance measurements in biomolecules: five-pulse double electron–electron resonance. *J Phys Chem Lett* 4(1):170-175.

89. Jeschke G, Bender A, Paulsen H, Zimmermann H, & Godt A (2004) Sensitivity enhancement in pulse EPR distance measurements. *J Magn Reson* 169(1):1-12.

90. Bode BE*, et al.* (2007) Counting the monomers in nanometer-sized oligomers by pulsed electron−electron double resonance. *J Amer Chem Soc* 129(21):6736-6745.

91. Endeward B, Butterwick JA, MacKinnon R, & Prisner TF (2009) Pulsed electron−electron double-resonance determination of spin-label distances and orientations on the tetrameric potassium ion channel KcsA. *J Amer Chem Soc* 131(42):15246-15250.

92. Milov AD & Tsvetkov YD (1997) Double electron-electron resonance in electron spin echo: conformations of spin-labeled poly-4-vinilpyridine in glassy solutions. *Appl Magn Reson* 12(4):495-504.

93. Manglik A, *et al.* (2015) Structural insights into the dynamic process of β2-adrenergic receptor signaling. *Cell* 161(5):1101-1111.

94. Chiang Y-W, Borbat PP, & Freed JH (2005) The determination of pair distance distributions by pulsed ESR using Tikhonov regularization. *J Magn Reson* 172(2):279-295.

95. Jeschke G, *et al.* (2006) DeerAnalysis2006-a comprehensive software package for analyzing pulsed ELDOR data. *Appl Magn Reson* 30(3-4):473-498.

96. Chiang Y-W, Borbat PP, & Freed JH (2005) Maximum entropy: a complement to Tikhonov regularization for determination of pair distance distributions by pulsed ESR. *J Magn Reson* 177(2):184-196.